

On the limiting geometry of unsteady breaking waves subject to co-flowing wind: spectrally-informed versus locally-measured steepness

Rui Cao^{1,2,3}, Enrique M. Padilla⁴, Xu Chen^{1,2} and Adrian H. Callaghan^{3,*}

¹State Key Laboratory of Physical Oceanography, Ocean University of China, Qingdao 266100, China

²College of Oceanic and Atmospheric Sciences, Ocean University of China, Qingdao 266100, China

³Department of Civil and Environmental Engineering, Imperial College London, London SW7 2AZ, UK

⁴Barcelona School of Industrial Engineering, Universitat Politècnica de Catalunya (UPC), Barcelona 08034, Spain

*Corresponding author: a.callaghan@imperial.ac.uk

27 May 2026

Abstract

Wave steepness is a key geometric variable for describing the occurrence of breaking and its consequences like energy dissipation and air entrainment. Using three laboratory campaigns under varying spectral conditions and co-flowing wind forcing, we contrast two types of steepness commonly employed for unsteady breaking waves: spectrally-informed wave-group steepness (prognostic), obtained from fixed-point surface-elevation records, and locally-measured crest steepness (diagnostic), obtained from surface spatial profiles extracted using the SDBW-I image-processing method developed herein. For the former, the long-adopted \mathcal{S}_n (linear sum of Fourier-component steepness) increases appreciably within approximately two dominant wavelengths upstream of breaking because of its strong sensitivity to evolving high-frequency content. When measured sufficiently far upstream, however, wave-group steepness remains approximately linearly related to the local zero-crossing steepness \mathcal{S}_b , across bulk unforced conditions. Notwithstanding this, we argue that the crest-front steepness, $\mathcal{S}_{\text{front}}(t_b)$, which delineates the slope of the front face at incipient breaking, is the most physically-meaningful metric among the steepness measures studied here. Specifically, it exhibits a consistent breaking-onset (lower-bound) threshold of $\mathcal{S}_{\text{front}}(t_b) \approx 0.2$, while its values above this threshold decrease with wind speed as crests become less forward leaning. This may be attributed to the combined effects of wind-modified dispersion, enhanced high-frequency spectral content and aerodynamic sheltering, suggesting that wind-wave and non-linear wave-wave interactions act as competing mechanisms in triggering breaking through kinematic and energetic processes beyond what geometry can explain. Even so, $\mathcal{S}_{\text{front}}(t_b)$ has strong potential as a controlling variable for future studies of breaking energetics and crest-scale dynamics.

1 Introduction

1.1 Broad motivation and background

Wave breaking is a discrete process occurring at the crests of sufficiently steep water waves, often in a seemingly random pattern in time and space. From a local perspective, breaking can

be viewed as the exceedance of a (geometric, kinematic, or dynamic) threshold beyond which the crest can no longer maintain its form or grow further (e.g. Johannessen and Swan, 2001; Wu and Nepf, 2002; Stansell and MacFarlane, 2002; Banner and Peirson, 2007; Toffoli et al., 2010; Knobler et al., 2022; Boettger et al., 2024; Hulin et al., 2025). In a broad context, identifying this limiting state when breaking occurs has implications for understanding air-sea exchanges of momentum and mass (e.g. generation of bubbles and sea spray), wave field development (e.g. limiting wave heights and wave energy dissipation), and turbulence generation that enhances upper ocean mixing (Melville, 1996; Duncan, 2001; Na et al., 2020; Deike, 2022; McAllister et al., 2024). Among the possible descriptors of this limiting state, wave steepness remains one of the most widely used geometric measures, although its definition and interpretation are not unique for unsteady breaking waves.

In the ocean, breaking rarely occurs without wind. Co-flowing wind supplies momentum and energy to the wave field through direct shear stress, involving both form drag and skin friction, and can thereby modify wave growth, crest steepening, and the occurrence of breaking (Miles, 1957; Hanson and Phillips, 1999; Olfateh et al., 2017; Babanin et al., 2018; Yousefi et al., 2024; Scapin et al., 2025). Around sufficiently steep crests, the overlying airflow may also separate, producing pressure asymmetry between the windward and leeward faces and altering the local forcing experienced by the crest (Jeffreys, 1926; Touboul et al., 2006; Buckley and Veron, 2016; Lee et al., 2017; Lee and Monty, 2020; Kristoffersen et al., 2021; Tan et al., 2025; Buckley et al., 2025). It is therefore reasonable to expect the limiting crest geometry at breaking to differ from that in unforced wave groups. However, because individual breaking events are difficult to isolate in the field, and because controlled wind-forced experiments remain relatively limited, how wind modifies the crest shape of unsteady breaking waves is still not well quantified.

The broad aim of the present work is therefore to examine how the limiting crest geometry of unsteady breaking waves varies across different unforced and wind-forced conditions, using wave steepness as the primary geometric measure.

1.2 Narrowing the problem

The definition of wave steepness, \mathcal{S} , usually involves a vertical and a horizontal length scale, but the particular choice of these scales varies across studies. Since most wind-driven oceanic breakers occur in unsteady wave groups, two approaches (types) have been developed to examine the breaking-wave steepness, as outlined below.

The first approach provides a diagnostic measure of the limiting crest geometry at incipient breaking¹. Following Derakhti et al. (2020) and Boettger et al. (2023), we note that this moment is different from breaking inception, which refers to the initiation of irreversible pre-breaking processes (e.g. non-linear dispersion, energy exchange, and local steepening) that eventually lead the wave to break. Measurements at incipient breaking therefore capture the limiting crest geometry in a wave that will break but before the crest overturns (McAllister et al., 2023, 2024). A commonly employed local measure is the zero-crossing steepness,

$$\mathcal{S}_b = a_b k_b \equiv a_b (2\pi/\lambda_b), \quad (1)$$

where a_b , k_b and λ_b are the local amplitude, wavenumber, and wavelength at incipient breaking, respectively (figure 1a). Reported values of \mathcal{S}_b for unsteady breakers can be below the Stokes limiting steepness $\mathcal{S} \approx 0.44$ for steady deep-water waves and can also vary with wave-group properties (Tian et al., 2010; Banner et al., 2014; Derakhti and Kirby, 2016; Saket et al., 2017; Barthelemy et al., 2018). Thus, although \mathcal{S}_b is useful, it does not define a unique geometric

¹This quantifies the limiting steepness attained by a crest at the instant of breaking where a vertical front face is present.

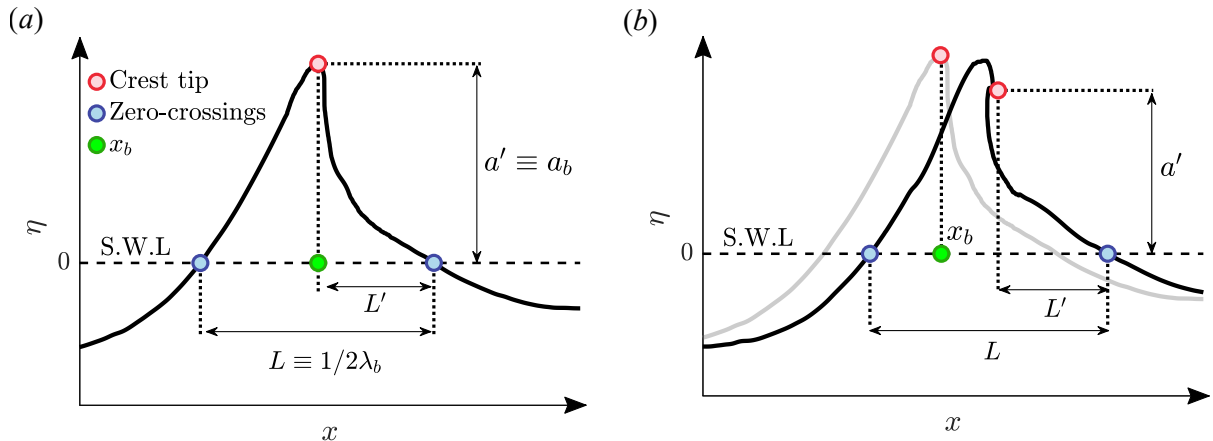


Figure 1. Illustrations of the parameters defining local crest geometry at (a) incipient breaking and (b) overturning. The wave propagates in the $+x$ direction. The profiles shown are from a real breaking event where its vertical dimension is exaggerated by a factor of 6.5 for clarity. In both panels, x_b marks the crest location at the brink of breaking, L the half-wavelength between zero crossings, and a' and L' the crest amplitude and crest-front distance, respectively, such that at incipient breaking $L = 1/2 \lambda_b$ and $a' = a_b$. The abbreviation, S.W.L., indicates the still water level.

breaking-onset threshold². Since breaking is often tied to the development of a forward-leaning crest (Fedele et al., 2020), other local measures concerning crest asymmetry and front-face slope may therefore be more directly connected to the limiting crest form (Kjeldsen and Myrhaug, 1979; She et al., 1994; Tian et al., 2008; Babanin et al., 2010; Perlin et al., 2013; De Vita et al., 2018; Chen and Zou, 2022; McAllister et al., 2023).

The second is what we refer to as wave-group steepness, computed from the wave group spectral composition measured upstream of the breaking location. This provides an *a priori* (prognostic) measure of group non-linearity and is widely used in laboratory and numerical studies because it can be obtained from single-point surface-elevation records, without tracking the rapidly evolving crest profile (Rapp and Melville, 1990; Drazen et al., 2008; Tian et al., 2010; Callaghan et al., 2013; Deike et al., 2015; Deane et al., 2016; Pizzo et al., 2021; Sinnis et al., 2021; Xu et al., 2022; Cui et al., 2022; Cao et al., 2023; McAllister et al., 2024).

Not only insightful in describing the breaking-wave steepening geometry and hence the degree of non-linearity, locally-measured and spectrally-informed steepness have often been used interchangeably as controlling variables for breaking-wave dynamics, energetics, and air entrainment (Rapp and Melville, 1990; Erinin et al., 2023, and among many others). In particular, wave-group steepness has been used to characterise the breaking strength of individual dispersively-focused laboratory breaking waves (Drazen et al., 2008; Sinnis et al., 2021; Cao et al., 2023), and has also been incorporated into spectral wave models to constrain the magnitude of the energy-dissipation source term (Romero, 2019; Hogan et al., 2025). These applications, however, implicitly assume that local crest steepness and spectrally-informed wave-group steepness are uniquely related.

Evidence for this assumption remains incomplete. One of the earliest studies in which a linear proportionality was reported came from Drazen et al. (2008), but we note that the two types of steepness they compared were not entirely independent and therefore contained a degree of self-correlation (see their figure 15). On the other hand, a linear relationship between \mathcal{S}_b and wave-group steepness (\mathcal{S}_n , defined later in equation (4)) was later reported in numerical and laboratory studies (Tian et al., 2010; Deike et al., 2016), but only for a limited set of dispersively-

²This defines the threshold magnitude of a steepness parameter required to trigger the least energetic breaking event.

focused breaking waves with constant-steepness spectra. Whether the same correspondence holds for more realistic oceanic spectra, such as JONSWAP, and across varying wave scales remains unresolved.

Furthermore, the action of direct wind forcing on wave group evolution leading to breaking may further complicate this correspondence. Indeed, laboratory experiments carried out in deep-water, wind-forced conditions have shown that sufficiently strong co-flowing wind can randomise the crest shape at incipient breaking (Oh et al., 2005; Babanin et al., 2010; Saket et al., 2017), with similar effects also reported numerically (Chen and Zou, 2022; Boettger et al., 2024). Otherwise, the wind influence on limiting wave steepness may not be measurable in general. For instance, the presence of positive vorticity, a possible consequence of wind-induced shear currents (Xie, 2017), has been shown to have little effect on limiting steepness (Touboul and Banner, 2021), although it may shift the breaking location downstream (Chen and Zou, 2022). These mixed findings motivate a systematic comparison of local and wave-group steepness under both unforced and wind-forced breaking conditions.

1.3 Target and expectation

Our study makes several contributions toward understanding the limiting geometry of breaking surface waves. We first present novel experimental datasets acquired in a state-of-the-art wind-wave flume in which a broad range of wind and wave-group conditions were concerned (§2.1–§2.3). Second, we introduce in §2.4 an image-processing method for extracting overturning crest profiles and the spatial parameters required to quantify local steepness. These measurements are combined with in-situ wave-gauge data to examine the along-flume evolution of spectrally-informed wave-group steepness (§3.1) and the temporal variation of locally-measured steepness (§3.2), and to contrast the two types of steepness without (§4.1) and with (§4.2) superimposed, co-flowing winds.

By doing so, we address whether spectrally-informed and locally-measured steepness can be used interchangeably under unforced and wind-forced breaking conditions, and clarify the physical interpretation of each when used to characterise unsteady breaking waves. We will also show that crest-front steepness (9) provides a more physically meaningful diagnostic of the limiting crest form, with implications for how wave scale and wind forcing are represented in studies of unsteady breaking waves. Our paper concludes with a synthesis of these findings and their broader implications (§5).

2 Experimental details and methods

2.1 General flume configuration

We employed laboratory-scale analogues to study individual oceanic breaking waves under both unforced and wind-forced conditions. The findings in the present study comprise results from three experimental campaigns (**SIREN**, **BUBER**, and **EURUS**), conducted between 2020 and 2021 in the unidirectional, wind–wave flume of the Hydrodynamics Laboratory within the Department of Civil and Environmental Engineering at Imperial College London.

The flume is 27 m long and 0.3 m wide, with transparent glass sidewalls for optical measurements. All experiments were conducted in freshwater at a fixed depth of $d = 0.7$ m. As shown in figure 2(a), paddle 1 generated the intermediate-to-deep-water wave groups, while paddle 2 behaved as an active dissipater by which incident energy was minimised. A parabolic beach made of 75% porosity plastic foam was installed next to paddle 2 to further reduce reflections.

Co-flowing wind was supplied at varying speed by a centrifugal wind generator mounted at the paddle-1 end of the flume. Air entered and exited through diffusers at both ends, with a

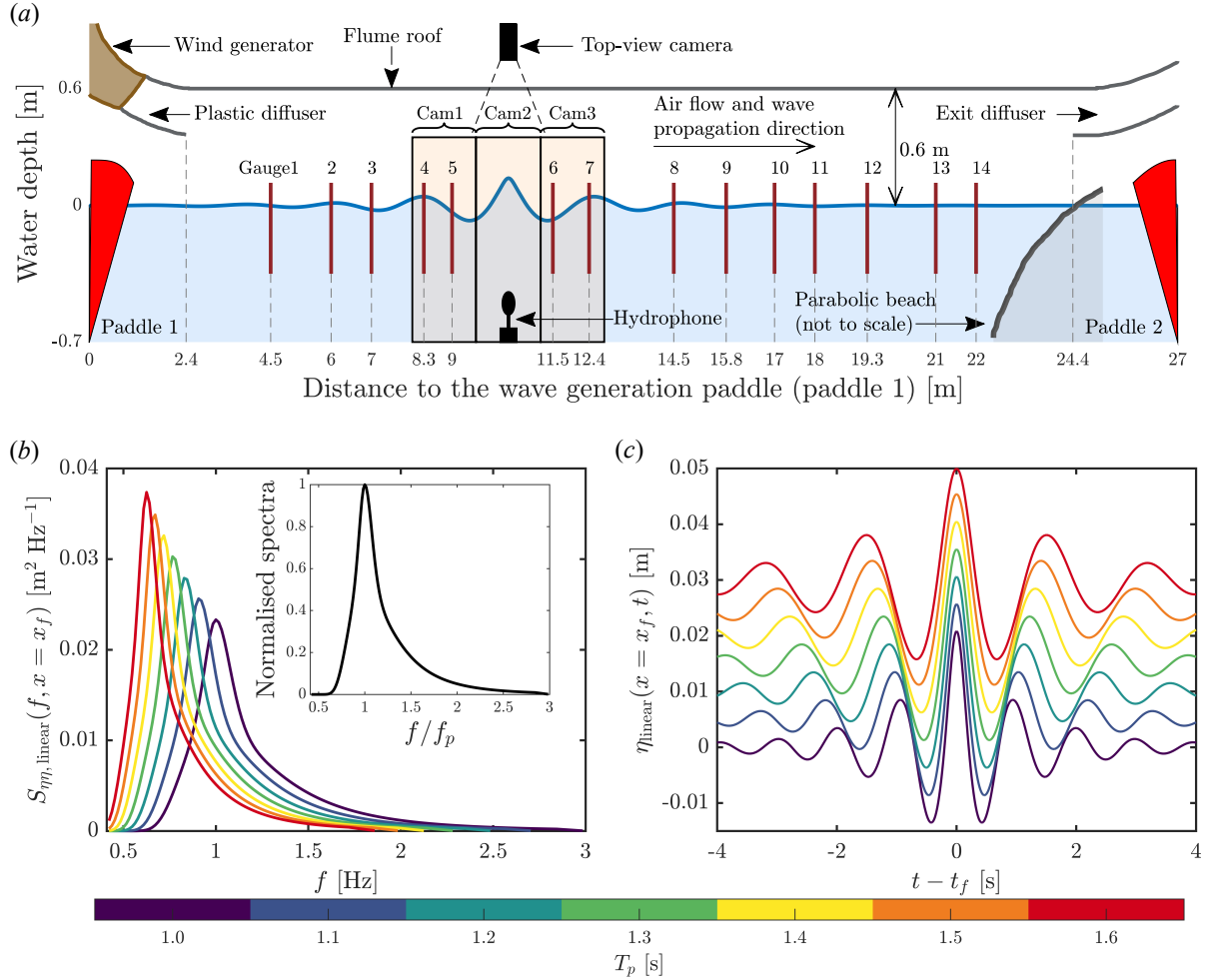


Figure 2. (a) Schematic of the experimental set-up for **SIREN**. An earlier version of this panel was published in [Cao et al. \(2026\)](#). (b, c) Target spectra ($S_{\eta\eta}(f) = a(f)^2/[2\delta f]$) and simulated surface elevations at the focal point for wave groups with equal $A = 20$ mm, $\gamma = 2$, and varying T_p . The inset in (b) shows the normalised spectra across different T_p values, with frequency f scaled by f_p and variance density normalised by $S_{\eta\eta, \text{linear}}(f = f_p, x = x_f)$. In (c), $\eta_{\text{linear}}(x, t)$ values for different T_p are vertically offset by $3A(T_p - 1)/2$. The colour bar underneath panels (b) and (c) indicates the T_p values used in **SIREN**.

vertical air space of 0.6 m between the still water level and the flume roof (although this height varied dynamically as waves propagated beneath the airflow).

2.2 Wave-group generation

All three campaigns employed dispersively focused wave groups generated from JONSWAP-type NewWave spectra using linear theory, following approaches commonly used to produce unsteady, air-entraining breaking waves (Rapp and Melville, 1990; Deane and Stokes, 2002; Drazen et al., 2008; Sinnis et al., 2021; Cao et al., 2023). This technique allows a nominal focusing time (t_f) and focusing location (x_f) of a steep crest to be prescribed. The target surface elevation, $\eta(x, t)$, is given by linear superposition of N freely propagating wave components, each of a specific frequency, f_i , and amplitude, a_i :

$$\eta(x, t) = \sum_{i=1}^N a_i \cos [k_i (x - x_f) - 2\pi f_i (t - t_f)], \quad (2)$$

where each frequency f_i is linked to its wavenumber k_i through the finite-depth dispersion relation, $(2\pi f_i)^2 = k_i g \tanh(k_i d)$, with g the gravitational acceleration. The target crest amplitude at the focal point is therefore the linear amplitude sum of all spectral components, $\eta_{\text{linear}}(x = x_f, t = t_f) = A = \sum_{i=1}^N a_i$.

Physical variables characterising the wave groups include the spectral peak period (T_p) and the JONSWAP peak enhancement factor (γ) of the designed spectra, for which wave scale and spectral bandwidth were independently varied: increasing T_p leads to an increased wavelength of the dominant spectral component, indicative of a larger wave scale (Callaghan et al., 2013; Cao et al., 2026); decreasing γ broadens the spectrum where the wave group is more dispersive and experiences a reduced degree of non-linear dispersion and wave-wave interaction compared to a correspondingly more narrowband wave group where frequency components have relatively more time to interact (Baldock et al., 1996; McAllister et al., 2023). In addition, wind forcing was applied at varying speeds, and the wind condition is expressed using the equivalent 10-m wind speed, \overline{U}_{10} , and the corresponding wave age, C_p/\overline{U}_{10} (Yousefi et al., 2024).

For each (T_p, γ, U_{10}) combination, sequences of wave groups with progressively increasing linear amplitude sum, A , were generated, ranging from quasi-linear, non-breaking waves to highly non-linear incipient breakers and ultimately plunging events (see table 1). In our experiments, only wave groups with a maximum of one breaking wave were analysed. When more than one breaking event occurred, A was either further increased to reproduce a single breaking event or the previous single-breaking case was retained. Although we note that the actual breaking location differed from the prescribed (x_f, t_f) and varied with A and wind speed, x_f and t_f in equation (2) were tuned so that each breaking event occurred within the field of view of Cam2 (see figure 2a).

All wave groups used a repeat time of 64 s, giving a frequency resolution of $\delta f = 1/64$ Hz. The underlying spectral range extended from 0.406 Hz (26/64 Hz, fixed) to $3/T_p$ ($= 3f_p$), so that the number of components was $N = (3/T_p - 26/64)/\delta f + 1$. For example, a wave group with $T_p = 1.2$ s comprised $N = 135$ individual spectral components.

For ease of reference, where needed, individual cases are labelled as x-GxTp α xxAxxx, in which the prefix denotes the campaign: **SIREN** (S), **BUBER** (N), and **EURUS** (H, for the highest wind speed applied). As an example, S-G3Tp13A020 refers to a wave group from **SIREN** with $\gamma = 3$, $T_p = 1.3$ s, and $A = 20$ mm.

| Campaign name | T_p [s] | γ | A [10^{-3} m] non-breaking | A [10^{-3} m] breaking | \overline{U}_{10} [m s^{-1}] | $\frac{C_p}{U_{10}}$ | N | $\tanh(k_p d)$ |
|---------------|-----------|----------|---------------------------------|-----------------------------|---|----------------------|-----|----------------|
| SIREN | 1.0 | 2 | 20–55 | 56–80 | n/a | n/a | 167 | 0.993 |
| | 1.1 | – | 20–56 | 64–110 | – | – | 149 | 0.982 |
| | 1.2 | – | 20–60 | 73–118 | – | – | 135 | 0.964 |
| | 1.3 | – | 20–81 | 96–146 | – | – | 122 | 0.942 |
| | 1.4 | – | 20–109 | 119–143 | – | – | 112 | 0.919 |
| | 1.5 | – | 20–113 | 134–154 | – | – | 103 | 0.891 |
| | 1.6 | – | 20–135 | 149–159 | – | – | 95 | 0.857 |
| | 1.1 | 3 | 20–57 | 64–110 | – | – | 149 | 0.982 |
| | 1.3 | – | 20–88 | 94–140 | – | – | 122 | 0.942 |
| | 1.5 | – | 20–124 | 130–154 | – | – | 103 | 0.891 |
| BUBER | 1.2 | 2 | 40–69 | 80–105 | 0 | No wind | 135 | 0.964 |
| | – | 3 | 40–71 | 83–117 | – | – | – | – |
| | 1.3 | 2 | 40–75 | 90–130 | – | – | 122 | 0.942 |
| EURUS | 1.2 | 2 | 40–69 | 80–105 | [3.0; 6.0] | [0.61; 0.30] | 135 | 0.964 |
| | – | 3 | 40–71 | 83–117 | – | – | – | – |
| | 1.3 | 2 | 40–75 | 90–130 | [3.0; 6.0] | [0.64; 0.32] | 122 | 0.942 |

Table 1. Summary of input linear target experimental conditions for **SIREN**, **BUBER** and **EURUS** campaigns. Columns indicate the spectral peak period (T_p), JONSWAP peak enhancement factor (γ), linear amplitude sum (A) for non-breaking and breaking cases, equivalent 10-m wind speed (\overline{U}_{10}), local wave age (C_p/\overline{U}_{10}), number of spectral components contained in a wave group (N), and finite-depth metric ($\tanh(k_p d)$).

2.3 Wave-group specifications and measurements

2.3.1 SIREN

The **SIREN** campaign was conducted in 2020 to investigate how breaking depends on wave scale.

The experimental arrangement is shown in figure 2(a). Along the flume centreline, 14 resistive wave gauges were deployed to record surface elevation at 128 Hz, of which five were placed upstream of the focal (breaking) zone and nine downstream. Three JAI GO series Charge-Coupled Device (CCD) cameras (Cam1–Cam3) imaged the crest evolution and the two-phase flow generated by breaking. Cam3 (the most downstream camera) was a 2.35-megapixel camera (1936 pixels \times 1216 pixels, with active area 11.3 mm \times 7.13 mm and cell size 5.86 μm \times 5.86 μm) equipped with a Tamron 12 mm lens and Cam1 and Cam2 were 5.1-megapixel cameras (2464 pixels \times 2056 pixels, with active area 8.50 mm \times 7.09 mm and cell size 3.45 μm \times 3.45 μm) equipped with Tamron 8 mm lenses. Together they covered approximately 4.5 m in the streamwise direction, from $x \simeq 8.0$ to 12.7 m. Illumination was provided by custom-built LED panels mounted opposite the cameras.

The cameras and light panels were synchronised using an Arduino-controlled trigger and operated at 52 Hz over a continuous 10 s recording window. This field of view and recording duration were sufficient to capture the full breaking process for the energetic groups considered here. The top-view camera and hydrophone shown in figure 2(a) are included for completeness but are not used in the present analysis (see Cao et al. (2026) for further details).

The conditions examined are summarised in table 1. Key parameters were varied over $T_p \in [1.0, 1.6]$ s, $\gamma \in [2, 3]$, and A , which was progressively increased from 0.02 m until a

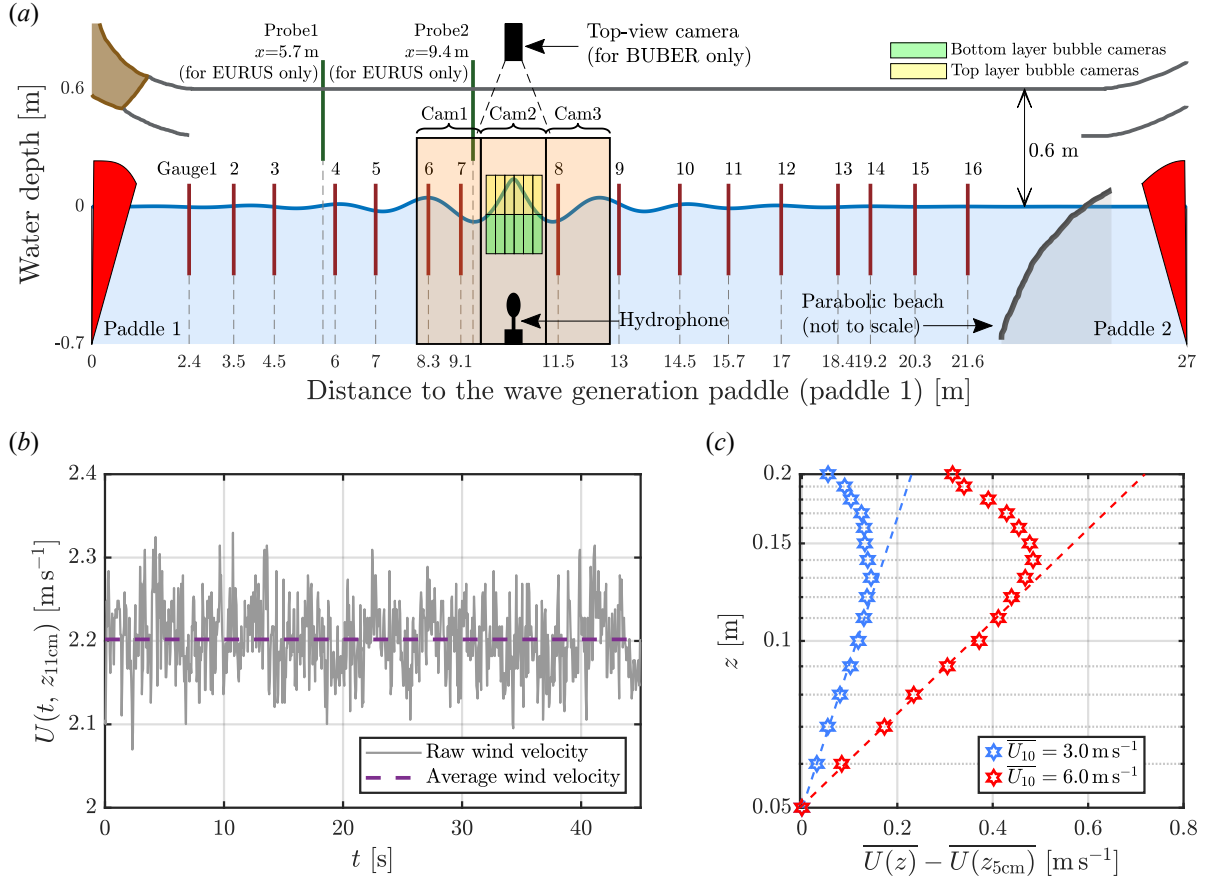


Figure 3. (a) Schematic of the experimental set-up for **BUBER** and **EURUS**. As in figure 2(a), all instruments are shown, although the hydrophone, top-view camera, and bubble-camera data are not used here. The top-view camera was used only in **BUBER**, while the two wind probes, located 5.7 m and 9.4 m from paddle 1, were used only in **EURUS**. (b) Time history of wind speed measured 0.11 m above the still water level for an extrapolated $\bar{U}_{10} = 3.0 \text{ m s}^{-1}$. (c) Vertical profiles of mean wind speed, $\bar{U}(z)$, for the two **EURUS** wind conditions, measured by wind probe 2; dashed lines show logarithmic fits.

controlled single breaking event could no longer be maintained within the field of view of Cam2. Figures 2(b, c) illustrate the target spectra and corresponding linear surface elevations for a representative subset of cases with $A = 20 \text{ mm}$ and $\gamma = 2$. The total spectral energy, $\int_{f_1}^{f_N} S_{\eta\eta}(f, x_f) df$, is identical for all the cases presented. As T_p increases the spectral peak shifts to lower frequency and the time-domain profile stretches horizontally, indicative of larger-scale wave groups. The inset in figure 2(b) shows that the normalised spectra retain the same shape across T_p , so that changes in wave scale are introduced without altering the prescribed spectral form.

2.3.2 BUBER and EURUS

Two further campaigns were conducted in 2021: **BUBER**, under unforced conditions, and **EURUS**, with direct co-flowing wind. They were designed to examine how wind forcing modifies the breaking process under otherwise comparable wave group conditions ($T_p \in [1.2, 1.3] \text{ s}$, $\gamma \in [2, 3]$; table 1).

The overall arrangement in **BUBER** was similar to **SIREN**, with several amendments (figure 3a). Sixteen wave gauges were installed along the flume, with seven upstream of the breaking zone and nine downstream. Cam1 and Cam3 were 2.35-megapixel cameras fitted with

Tamron 12 mm lenses, while Cam2 was a 5.1-megapixel camera fitted with a Tamron 8 mm lens. Additional 5.1-megapixel cameras were employed to image bubble plumes (regions shaded by yellow and green colours), although those data are not analysed here. All cameras operated at 20 Hz with LED backlighting.

For **EURUS**, the flume was fully sealed to prevent air leakage along the flume between the air inflow and outflow locations. Two piezoelectric wind probes (TSI 8455-075-1, 20 Hz) were installed at fetches of 5.7 m and 9.4 m from paddle 1. Wind speeds from the downstream probe were used because this location was immediately upstream of the breaking zone and therefore more representative of the local airflow conditions. Before each focused wave group was generated, the wind was allowed to blow for 8 minutes to establish a statistically steady background wave field with small, high-frequency ripples (see also appendix A.1 for measurements on these purely wind-induced wave fields).

The characteristic wind speed is taken as the equivalent 10-m velocity (\overline{U}_{10}), extrapolated from logarithmic profiles measured under statistically steady, wind-only conditions:

$$U(x, z) = \frac{u_*}{\kappa} \ln \left[\frac{z}{z_0(x)} \right], \quad (3)$$

where $\kappa = 0.41$ is the non-dimensional von Karman constant, u_* is the friction velocity, and z_0 is the roughness length. The values of u_* and z_0 were computed by fitting equation (3) to the measured wind profiles.

Figure 3(b) shows an example wind speed time history at $z = 0.11$ m, averaged over 45 s. The mean profiles measured by probe 2 for the two **EURUS** wind conditions, $\overline{U}_{10} = 3.0$ and 6.0 m s^{-1} , are shown in figure 3(c). Measurements were taken from $z = 0.05$ to 0.2 m, avoiding positions too close to the free surface to protect the probe and reduce Wave Boundary Layer (WBL) effects (Chalikov and Rainchik, 2011). Because the wind speed decreases above approximately $z = 0.13$ m (mainly due to momentum loss associated with the flume roof), only data up to this height were used for the logarithmic fits and for extrapolating \overline{U}_{10} .

Alongside underlying wave group conditions, the airflow conditions for **BUBER** and **EURUS** are summarised in table 1 using \overline{U}_{10} and the wave age C_p/\overline{U}_{10} . Although mechanically generated wave groups may perturb the airflow, especially at larger steepness, these values are used as representative indicators of the intended young and very young wind-wave regimes.

Before presenting the results for breaking wave groups, we first examine in appendices A.1–A.2 purely wind-induced waves and wind-forced non-breaking groups, through which the physical context for interpreting breaking-wave results is established (appendix A.3).

2.4 Extraction of surface profile at incipient breaking and overturning

Quantifying local wave steepness requires the air–water interface to be extracted accurately from side-view images. In our earlier work (Cao et al., 2025), we introduced the Continuous Maximum Gradient (CMG) method, in which the free surface is treated as a smooth streamline of connected pixels. This method is robust for non-breaking waves, but becomes inadequate once the crest overturns, because the interface then contains near-vertical segments and multi-valued profiles that break down the streamline hypothesis we made in CMG.

In resolving this limitation, we implement Phase I of the Surface Detection for Breaking Waves method (SDBW-I) developed in Cao (2024). The full SDBW framework distinguishes four optical phases of breaking; only Phase I is required here as it resolves the transition from incipient breaking, where a near-vertical front face is present, to early crest overturning.

The procedure of SDBW-I is illustrated in figure 4. After image calibration and pre-

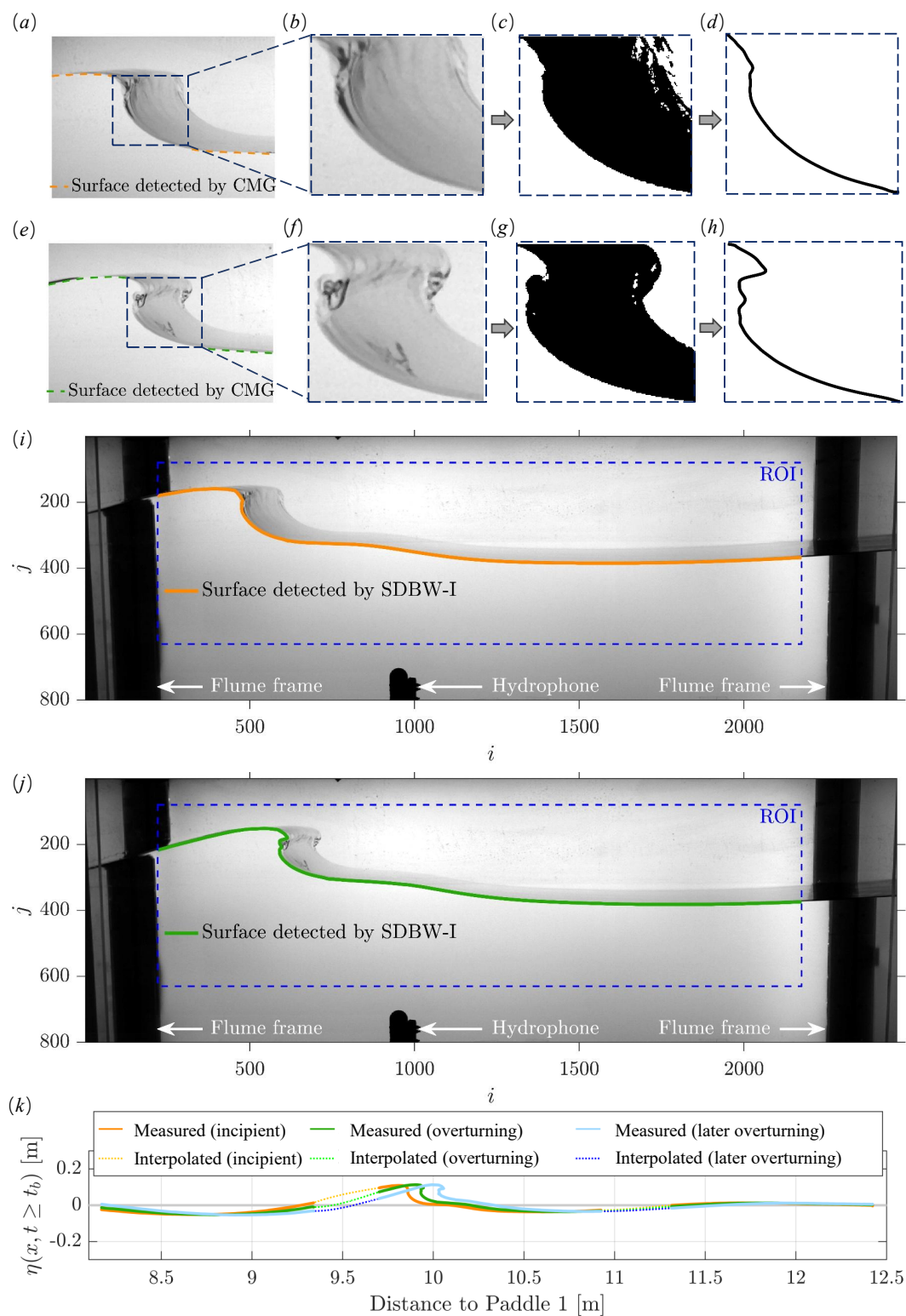


Figure 4. Mechanics and performance of SDBW-I. The first and second rows correspond to incipient breaking (vertical front face) and overturning, respectively: (a, e) snapshots of case S-G2Tp12A095 with partial CMG detection; (b, f) zoomed-in regions; (c, g) binary images from Otsu threshold; and (d, h) extracted air–water interface along the inner face of the crest. (i, j) SDBW-I detection compared with Cam2 imagery, in pixel i - j coordinates. (k) Combined surfaces from three cameras in real-world coordinates with equal axes scales. Dotted lines denote the interpolation (S -interp, Padilla et al., 2023) across gaps obscured by flume frames, as seen in figures 4(i) and 4(j).

processing following [Cao et al. \(2025\)](#), a rectangular Region of Interest (ROI) is defined around the steepening or overturning crest, while the neighbouring non-breaking portions of the free surface are still detected using CMG (figures 4*a*, *e*). The ROI is then converted to a binary image using Otsu thresholding (figures 4*b*, *f* → figures 4*c*, *g*), and the multi-valued interface is identified from the pixels forming the inner face of the crest (figures 4*c*, *g* → figures 4*d*, *h*). Since the waves propagate rightward, this interface is consistently taken as the left-hand boundary of the binary crest region. Combining this SDBW-I detection with the non-breaking portions extracted by CMG yields the complete surface profile within the camera field of view (figures 4*i*, *j*).

The interface detected is then mapped from pixel coordinates (i, j) to physical coordinates (x, z) to obtain $\eta(x, t)$. This transformation accounts for perspective effects arising from the non-perpendicular alignment of the camera optical axis relative to the x - z plane of the wave flume, which introduces position-dependent scaling across the image. Lens distortion is removed through intrinsic calibration, while the remaining perspective-induced scaling variations are corrected using modified extrinsic parameters, following the procedures described in [Cao \(2024\)](#). This provides spatially consistent surface profiles across the measurement domain.

Figure 4(*k*) shows the transformed surface elevations from the three cameras at incipient breaking and during overturning. Gaps between adjacent camera views, caused by the flume metal struts, are interpolated using S -interp ([Padilla et al., 2023](#)). These reconstructed profiles provide the geometric basis for tracking the temporal evolution of local steepness (§3.2).

3 Evolution of wave-group steepness and local steepness

3.1 Wave-group steepness

Spectrally-informed measures of wave-group steepness are derived from surface-elevation time histories, but their values can depend on where the measurements are made. As a focused wave group approaches breaking, rapid spectral evolution (especially in the high-frequency components) can modify the steepness inferred from the measured spectrum ([Derakhti and Kirby, 2014](#); [Cao et al., 2023](#)).

In our previous work ([Cao et al., 2023](#)), we compared several definitions of wave-group steepness between a far upstream location and a point immediately upstream of breaking where non-linearity was strong. That study, however, was limited in wave scale and did not include wind forcing. Here we focus on three metrics commonly used ([Cao et al., 2023](#)), briefly reintroduced below, and extend the analysis by examining their along-flume evolution across a broader range of wave scales and under direct co-flowing wind.

3.1.1 Definitions and interpretation

The first is the linear superposition of the steepness of all spectral components,

$$\mathcal{S}_n = \sum_{i=1}^N a_i k_i. \quad (4)$$

Introduced by [Melville \(1994\)](#), \mathcal{S}_n has been widely used as a prognostic measure of (linear) maximum steepness in deterministic breaking-wave studies (e.g. [Drazen et al., 2008](#); [Sinnis et al., 2021](#)).

The second metric scales the linear amplitude sum with the wavenumber at the spectral peak,

$$\mathcal{S}_p = k_p \sum_{i=1}^N a_i \equiv k_p A, \quad (5)$$

where k_p corresponds to the peak frequency f_p through the linear dispersion relation. This definition is most appropriate for wave groups with a well-defined spectral peak (Cao et al., 2023).

The third metric incorporates a spectral energy-weighted frequency f_s :

$$f_s = \frac{\sum_{i=1}^N (f_i a_i^2) (\delta f)_i}{\sum_{i=1}^N (a_i^2) (\delta f)_i}, \quad (6)$$

with the corresponding steepness defined as:

$$\mathcal{S}_s = k_s \sum_{i=1}^N a_i \equiv k_s A, \quad (7)$$

where k_s is the wavenumber associated with f_s . Previous studies have shown that \mathcal{S}_s scales approximately linearly with the locally measured breaking steepness \mathcal{S}_b (equation (1)) (Tian et al., 2010; Cui et al., 2022). Compared with \mathcal{S}_n and \mathcal{S}_p , it has also been found to provide stronger predictive skill for breaking onset and improved collapse when characterising breaking strength, owing to its explicit dependence on the spectral energy distribution (Derakhti and Kirby, 2016; Cao et al., 2023).

3.1.2 Effects of wave scale and bandwidth

Figure 5 illustrates the spatial evolution of \mathcal{S}_p , \mathcal{S}_s , and \mathcal{S}_n for a selection of wave groups with varying wave scale (a – c), spectral bandwidth (d – f), and wind-forcing conditions (g – i). Both breaking and non-breaking cases are included. The streamwise coordinate is expressed relative to the focal/breaking location x_b and normalised by the spectral peak wavelength λ_p , such that negative and positive values of $(x - x_b)\lambda_p^{-1}$ correspond respectively to upstream and downstream measurements.

A clear dependence on wave scale is observed in figures 5(a)–(c). For otherwise identical conditions, wave groups with larger T_p have smaller values of all three steepness metrics. This follows from the shift of the spectral peak to lower frequency as T_p increases: the dominant wavelength becomes longer, and the same linear amplitude sum A therefore corresponds to a less steep wave group. By contrast, varying γ within the limited range tested here produces no measurable change in the wave-group steepness evolution (figures 5(d)–(f)).

For both breaking and non-breaking cases without wind forcing (figures 5(a)–(f)), the three metrics remain relatively constant until approximately two dominant wavelengths ($\sim 2\lambda_p$) upstream of x_b . Closer to breaking, \mathcal{S}_n increases, due to its heavier weighting of high-frequency components and their rapid evolution during non-linear focusing, as discussed in Cao et al. (2023). Immediately downstream of x_b , all three metrics decrease abruptly, consistent with breaking-induced energy loss, and then continue to decay as the wave groups disperse and sidewall frictional dissipation takes effect.

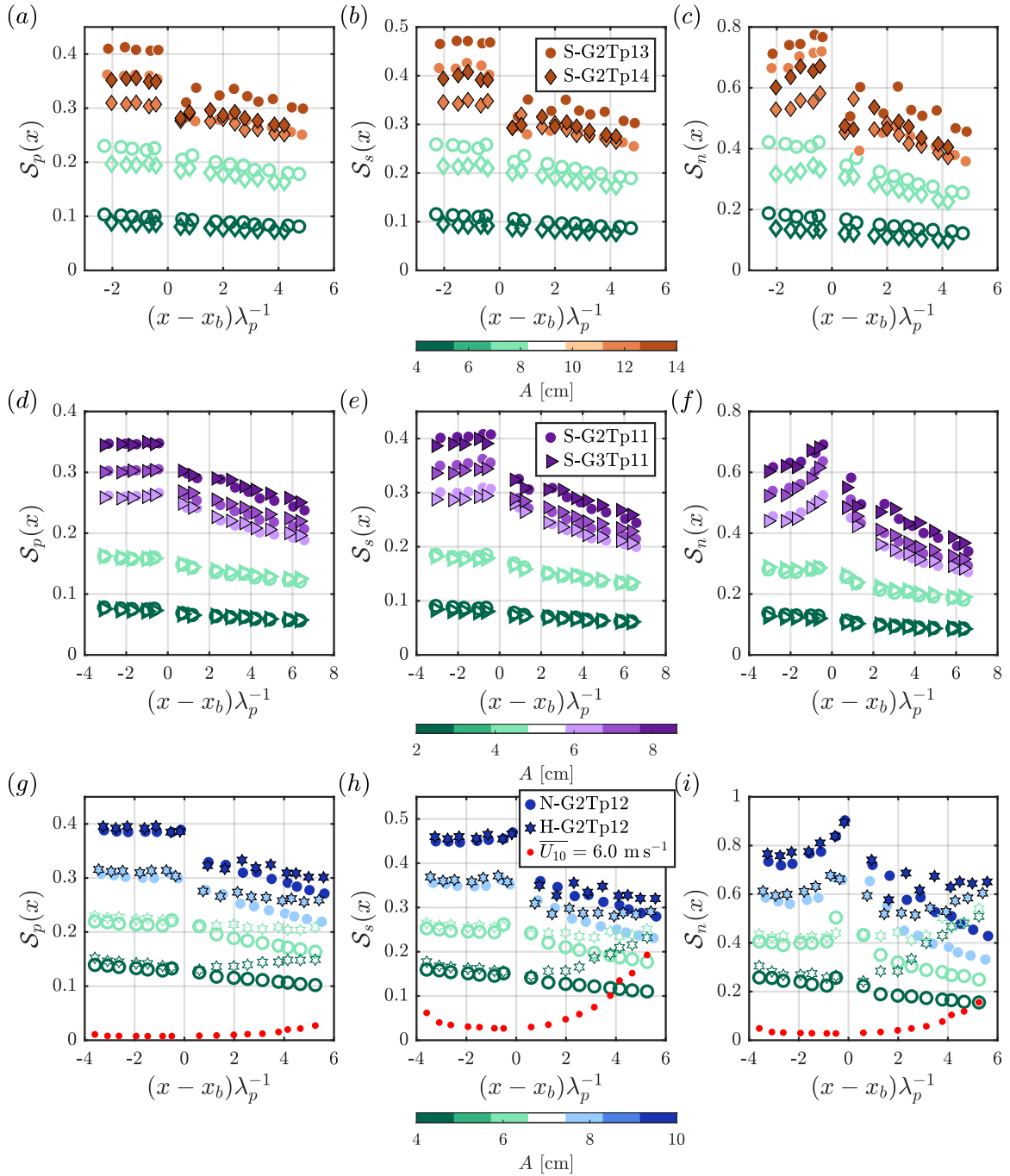


Figure 5. Spatial evolution of the three spectrally-informed wave-group steepness measures upstream and downstream of the focal/breaking locations. In each panel, hollow and filled symbols denote non-breaking and breaking wave groups, respectively, with colour indicating the linear amplitude sum A . Panels (a)–(c) show **SIREN** cases with $\gamma = 2$ and varying wave scale; panels (d)–(f) show **SIREN** cases with fixed $T_p = 1.1$ s and different spectral bandwidths; and panels (g)–(i) show **BUBER** and **EURUS** cases with $\gamma = 2$, $T_p = 1.2$ s, and either no wind or co-flowing wind ($C_p/\overline{U}_{10} \approx 0.3$). Red dots in panels (g)–(i) denote steepness values of purely wind-generated waves at $\overline{U}_{10} = 6.0$ m s $^{-1}$.

3.1.3 Effect of wind

We next consider the effect of co-flowing wind. Figures 5(*g*)–(*i*) compare \mathcal{S}_p , \mathcal{S}_s , and \mathcal{S}_n between unforced wave groups from **BUBER** and wind-forced wave groups from **EURUS**. It is seen that wind increases all three metrics, but only slightly upstream of x_b . This is because, over the relatively short fetch upstream of breaking, wind input adds limited energy within the spectral range used to compute these steepness metrics (see also figures 13 and 14, appendix A.1). For reference, we show in the red dots the corresponding steepness values of purely wind-generated waves at $\overline{U}_{10} \approx 6.0 \text{ m s}^{-1}$.

Downstream of x_b , the wind effect becomes more pronounced, especially for wave groups with smaller A and at longer fetches (similar to those seen in purely wind-induced wave fields as represented by red dots). As A increases and the mechanically generated wave groups become more energetic, the relative contribution from wind weakens, suggesting that the added wind input is less important compared with the paddle-wave energy. This reduced influence is also consistent with the background-wave suppression mechanism of Touboul et al. (2006), in which long paddle-generated waves interact with but inhibit the growth of shorter wind waves. These shorter components are then more readily dissipated by sidewalls and, in some cases, fall outside the frequency band used in the steepness calculation. We return later in §3.1.5 to discuss how different metrics of wave group steepness respond to the choice of upper frequency limit.

3.1.4 Global comparison

We now compare wave-group steepness measured near the wavemaker with that measured just upstream of x_b for the full dataset (figures 6*a–c* for **SIREN** and figures 6*d–f* for **BUBER** and **EURUS**). This tests whether the spatial trends identified above persist across different wave scales, bandwidths, and wind conditions. Note that we denote the **SIREN** gauges using χ to distinguish them from those in **BUBER** and **EURUS**; specifically, χ_1 ($\simeq 4.5 \text{ m}$) and χ_5 ($\simeq 9.0 \text{ m}$) have fetch distances comparable to x_3 and x_7 , respectively (see also figures 2*a* and 3*a*).

The results presented in figure 6 confirm that across the bulk of the data only \mathcal{S}_n exhibits a measurable spatial dependence: steeper and thus more energetic wave groups experience a noticeable increase in \mathcal{S}_n as they propagate towards x_b , whereas \mathcal{S}_p and \mathcal{S}_s remain comparatively insensitive to measurement location. This dependence is broadly independent of spectral bandwidth, wave scale, and wind forcing. Comparing figures 6(*c*) and 6(*f*) also shows that \mathcal{S}_n measured just upstream of x_b is slightly higher for **BUBER** and **EURUS** than for **SIREN**. This is because the breaking location x_b in **EURUS** and **BUBER** was shifted slightly upstream, demonstrating again the sensitivity of \mathcal{S}_n to the non-linear evolution of propagating wave groups.

This sensitivity has a practical implication. If wave-group steepness is to be used as a prognostic indicator of local breaking steepness or breaking strength, it should not be evaluated too close to the breaking point. Under the present conditions, measurements taken more than approximately two dominant wavelengths upstream of x_b are needed to avoid contamination by local non-linear growth (as shown in figure 5, right column).

3.1.5 Implications for the use of different wave-group steepness metrics

As noted earlier (and also described in appendices A.2–A.3), upstream of x_b the wind mainly increases the energy of the spectral components above the upper frequency limit used in the default steepness calculations ($f_N = 3f_p$), where shorter wind-induced waves reside. This raises the question of whether the relative invariance in wave-group steepness between wind-unforced and wind-forced conditions is simply a consequence of restricting the integration band to $3f_p$.

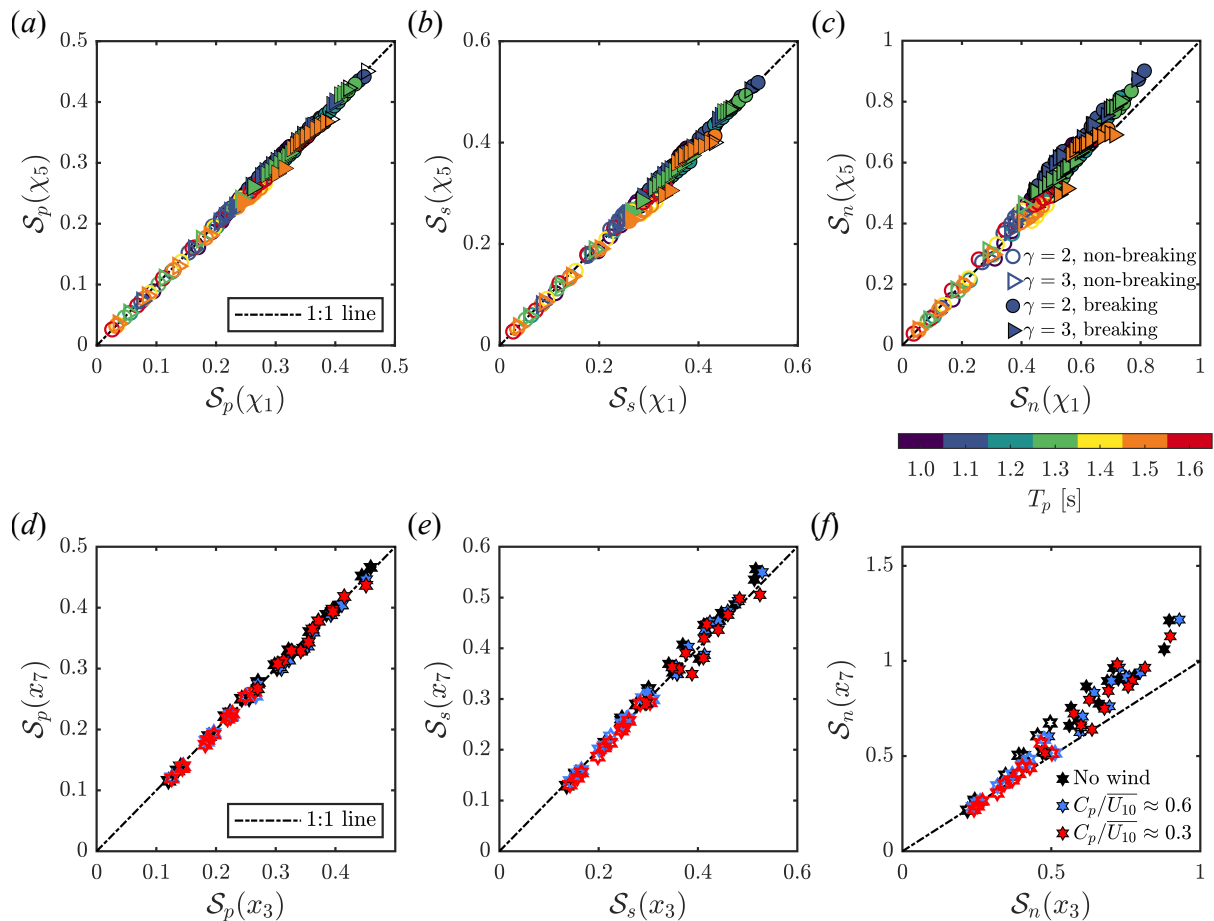


Figure 6. (a)–(c) Comparisons of S_p , S_s , and S_n between the most upstream location (χ_1) and a location just upstream of x_b (χ_5) for all non-breaking and breaking waves from **SIREN**. (d)–(f) Equivalent comparisons for breaking cases from **BUBER** and **EURUS**, using x_3 and x_7 , whose fetch distances are comparable to $\chi_1 = 4.5$ m and $\chi_5 = 9.0$ m in **SIREN** (see figures 2a and 3a).

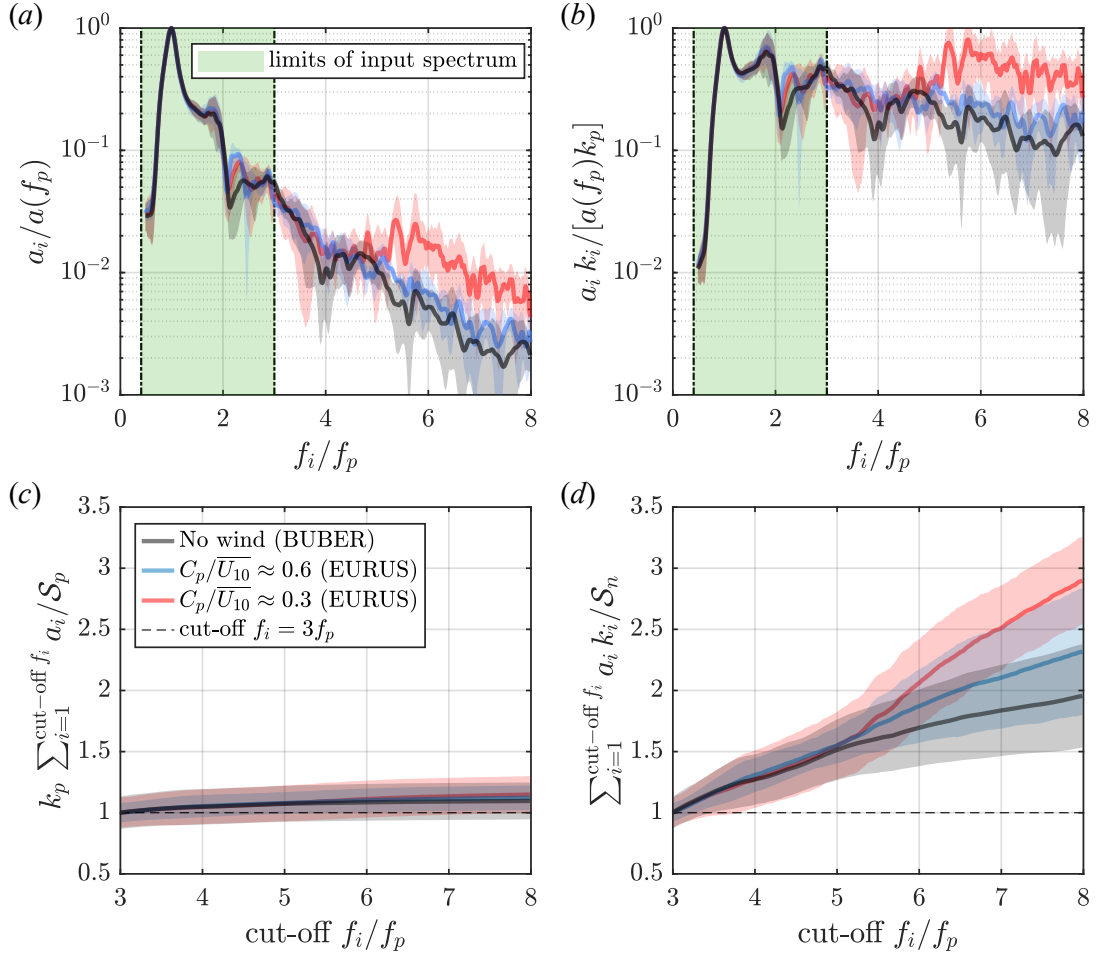


Figure 7. (a, b) Spectrally resolved distributions of \mathcal{S}_p and \mathcal{S}_n at $x_7 = 9.1$ m, just upstream of breaking. Values are normalised by their respective peaks, and shaded green regions mark the prescribed paddle-wave generation range. (c, d) Cumulative spectrally resolved wave-group steepness as the cut-off frequency is progressively extended, normalised by the reference values at $f_i/f_p = 3$ (horizontal dashed lines). Results are ensemble averages of four G2Tp12 breaking events ($\gamma = 2$, $T_p = 1.2$ s) under unforced (**BUBER**) and wind-forced conditions ($C_p/\overline{U}_{10} \approx 0.6$ and $C_p/\overline{U}_{10} \approx 0.3$, **EURUS**). Shaded bands indicate ± 1 standard deviation from ensemble means.

To examine this, we consider \mathcal{S}_p and \mathcal{S}_n for four breaking events with $\gamma = 2$ and $T_p = 1.2$ s under different wind speeds (\mathcal{S}_s is not shown because it behaves similarly to \mathcal{S}_p). Their spectrally resolved distributions at x_7 are shown in figures 7(a) and 7(b). These distributions are normalised by their respective peak values, so for \mathcal{S}_p it simplifies to $a_i k_p / [a(f_p) k_p] \rightarrow a_i / a(f_p)$. Two points stand out. First, within the prescribed paddle-wave band, wind has little effect on either metric, consistent with figures 5(g) and 5(i). Second, clear difference appears in the high-frequency tail. For \mathcal{S}_p (figure 7a), the wind-induced contribution remains one to two orders of magnitude smaller than that from the main band. For \mathcal{S}_n (figure 7b), however, the same high-frequency contribution can become comparable to, or even exceed, the main-band contribution because of the stronger weighting by higher wavenumber.

This contrast is further quantified in figures 7(c) and 7(d), which show the cumulative spectrally-resolved steepness as we progressively extend the cut-off frequency. The reference cut-off, $f_i = 3f_p$, corresponds to the default range used to compute \mathcal{S}_p and \mathcal{S}_n . Broadly speaking, the value of \mathcal{S}_p is largely insensitive to this choice: extending the cut-off to $8f_p$ changes it by less than 10%. By contrast, \mathcal{S}_n increases rapidly, becoming about 50% larger by $5f_p$. Beyond this point, wind effects become increasingly apparent; at $8f_p$, \mathcal{S}_n under the strongest wind condition can be nearly twice its reference value at $3f_p$.

The implication here is worth emphasising. In the presence of wind forcing, unconstrained spectral integration (or summation) can imply artificially high wave-group steepness near breaking, even when this increase arises mainly from small but cumulative energy in the high-frequency tail. This represents an important limitation of spectrally-informed steepness metrics under wind, particularly for \mathcal{S}_n . We therefore turn next to locally-measured steepness (§3.2) and examine how it compares with these spectral measures (§4).

3.2 Local steepness

As introduced in §1.2, local steepness differs from spectrally-informed steepness in that it is a diagnostic parameter, and one that quantifies the pre-breaking processes that lead up to wave breaking. Following equation (1), we first define a generic locally measured zero-crossing steepness from the geometric quantities shown in figure 1:

$$\mathcal{S}_{zc}(t) = \frac{\pi a'(t)}{L(t)}. \quad (8)$$

At incipient breaking ($t = t_b$), $\mathcal{S}_{zc}(t_b) \equiv \mathcal{S}_b$. Additionally, we define a more localised steepness for the crest front face:

$$\mathcal{S}_{\text{front}}(t) = \frac{a'(t)}{L'(t)}, \quad (9)$$

which characterises the forward-leaning front face commonly observed as breaking is approached, when the front-face slope becomes much larger than that of the rear face (see Perlin et al. (2013) and the example in figure 4).

These local steepness metrics are quantified from the SDBW-I surface reconstructions described in §2.4. Figure 8 shows the temporal evolution of \mathcal{S}_{zc} and $\mathcal{S}_{\text{front}}$ for an ensemble of five **BUBER** breaking waves with similar wave-group steepness \mathcal{S}_n .

Both local steepness metrics show a broadly similar trend: they increase as the crest steepens towards breaking and decay rapidly after t_b . Their maxima occur at incipient breaking, consistent with local steepness acting as a diagnostic measure of crest evolution. After breaking, the crest loses its coherent form and no longer steepens. These results provide a useful reference for §4, where we compare local and wave-group steepness under different wave and

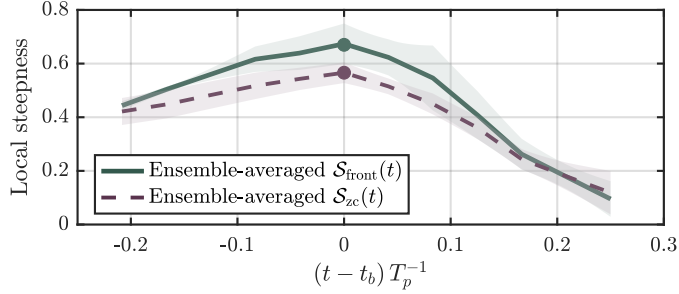


Figure 8. Time-evolving histories of the locally-measured zero-crossing steepness, $\mathcal{S}_{zc}(t)$, and crest-front steepness, $\mathcal{S}_{\text{front}}(t)$, before and after incipient breaking at t_b . Results are ensemble averages over five **BUBER** breaking waves with similar \mathcal{S}_n . Shaded regions indicate ± 1 standard deviation, and solid points at $(t - t_b)/T_p = 0$ mark values of local steepness at incipient breaking.

wind conditions.

4 Relationships between locally-measured and spectrally-informed steepness

4.1 Comparison across wave scales in the absence of direct wind stress

4.1.1 \mathcal{S}_b versus different measures of wave-group steepness

In the left panels of figure 9, the locally-measured zero-crossing steepness at incipient breaking, \mathcal{S}_b , is compared with the three upstream wave-group steepness metrics, $\mathcal{S}_p(\chi_1)$, $\mathcal{S}_s(\chi_1)$, and $\mathcal{S}_n(\chi_1)$, for all **SIREN** breaking cases. Despite variations in T_p and γ , \mathcal{S}_b remains strongly correlated with all three metrics. Following [Drazen et al. \(2008\)](#) and [Tian et al. \(2010\)](#), we quantify these relationships using simple linear fits:

$$\mathcal{S}_b = (1.77 \pm 0.15)\mathcal{S}_p(\chi_1) - (0.13 \pm 0.05), \quad R^2 = 0.83, \quad (10)$$

$$\mathcal{S}_b = (1.54 \pm 0.15)\mathcal{S}_s(\chi_1) - (0.11 \pm 0.06), \quad R^2 = 0.80, \quad (11)$$

and

$$\mathcal{S}_b = (0.92 \pm 0.09)\mathcal{S}_n(\chi_1) - (0.08 \pm 0.05), \quad R^2 = 0.80. \quad (12)$$

These trends are broadly consistent with previous reports of near-linear \mathcal{S}_b - \mathcal{S}_n scaling ([Drazen et al., 2008](#); [Deike et al., 2016](#)) (noting, however, that the definitions of \mathcal{S}_b and \mathcal{S}_n differ slightly between studies), and with reported \mathcal{S}_b - \mathcal{S}_s scaling ([Tian et al., 2010](#); [Cui et al., 2022](#)).

The grouping of the present data onto near-linear relations indicates that, in the absence of wind forcing, wave-group steepness measured sufficiently far upstream of breaking can serve as a useful predictor of the local zero-crossing steepness at incipient breaking. This remains the case even for \mathcal{S}_n , despite its stronger sensitivity to high-frequency spectral content compared with \mathcal{S}_p and \mathcal{S}_s .

4.1.2 $\mathcal{S}_{\text{front}}(t_b)$ versus different measures of wave-group steepness

When the crest-front steepness at incipient breaking, $\mathcal{S}_{\text{front}}(t_b)$, is used in place of \mathcal{S}_b , the influence of wave scale becomes evident (figure 9, right panels). Larger-scale wave groups with larger T_p need to become more non-linear, and therefore reach higher wave-group steepness, to attain the same level of $\mathcal{S}_{\text{front}}(t_b)$ as lower- T_p wave groups. As a result, the spectrally-informed steepness measures do not collapse the limiting front-face geometry in the same way as they do

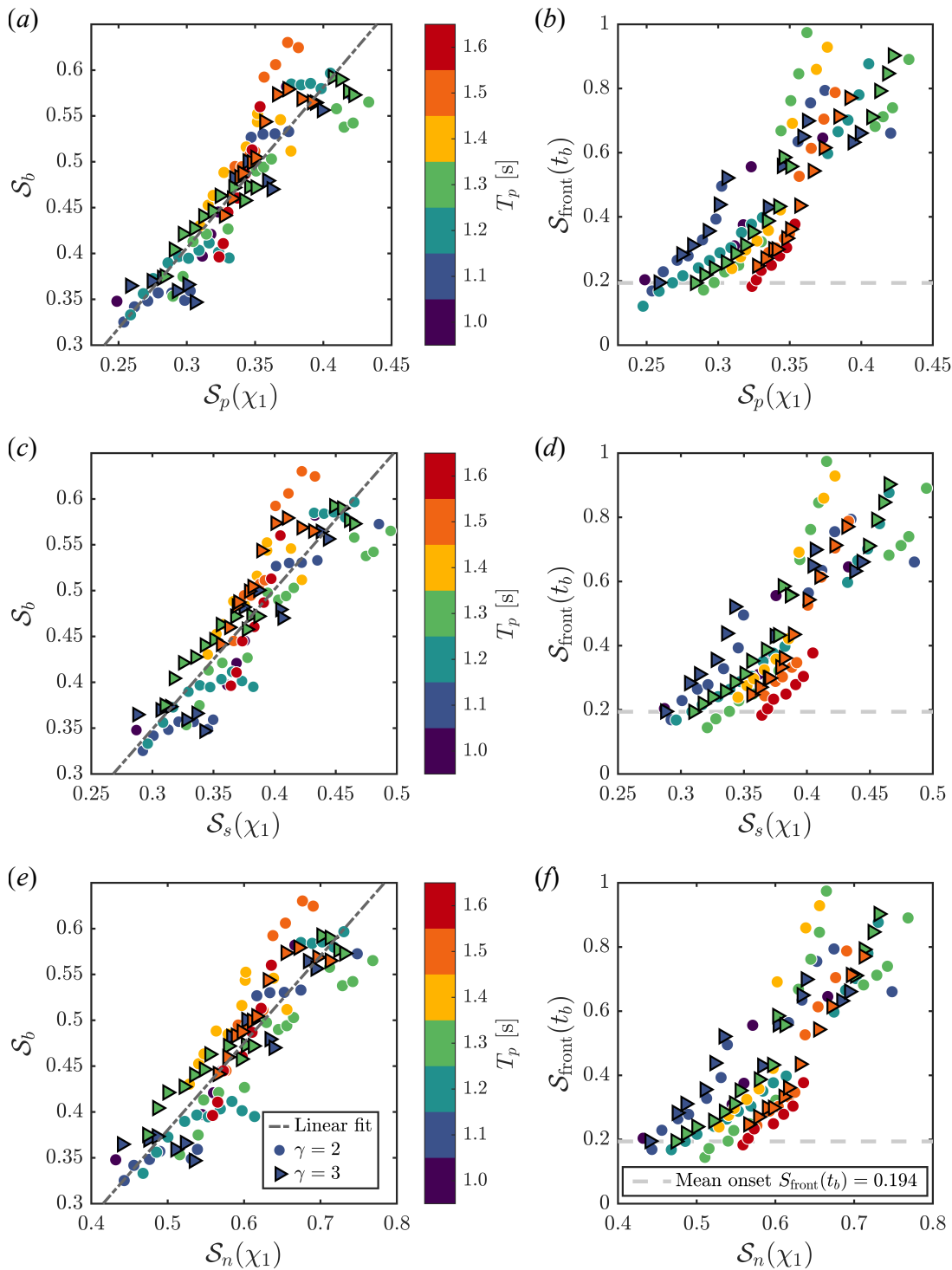


Figure 9. Comparisons between local crest steepness at incipient breaking (S_b , left column, and $S_{\text{front}}(t_b)$, right column) and upstream wave-group steepness ($S_p(\chi_1)$, $S_s(\chi_1)$ and $S_n(\chi_1)$) for **SIREN** breaking cases across different wave scales and spectral bandwidths. Dash-dotted lines in the left panels show linear least-squares fits. Grey dashed lines in the right panels indicate the average minimum value of $S_{\text{front}}(t_b)$ required for breaking within the tested conditions, i.e. the breaking-onset threshold.

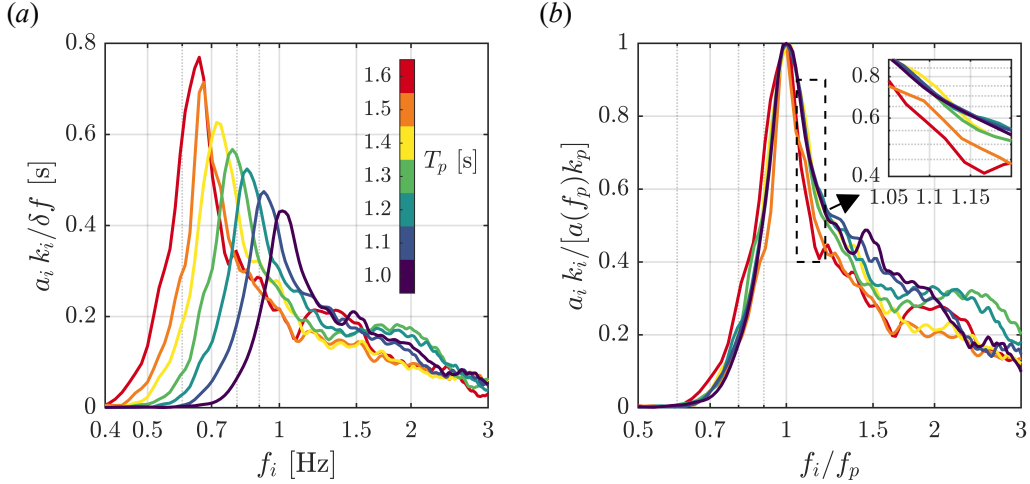


Figure 10. Measured spectrally-resolved steepness distributions of Fourier-decomposed components for the **SIREN** $\gamma = 2$ (non-breaking) wave groups with varying T_p but comparable wave-group steepness $S_n(\chi_1) \in [0.30, 0.35]$. Panel (a) shows the absolute steepness density, $a_i k_i / \delta f$, as a function of frequency, and panel (b) shows the corresponding distributions normalised by the spectral peak, $a_i k_i / [a(f_p) k_p]$, as a function of the normalised frequency f_i / f_p .

for \mathcal{S}_b .

The above scale dependence may be explained by differences in the spectral steepness distributions among wave groups with different T_p . To demonstrate this we show in figure 10 selected **SIREN** cases with comparable measured wave-group steepness $S_n(\chi_1) \in [0.30, 0.35]$, but different T_p . As T_p decreases, the dominant steepness contribution shifts towards higher frequencies (figure 10a). This matters because high-frequency components are particularly relevant to crest instability and hence to the occurrence of breaking (Cao et al., 2023). Indeed, although the variance-density spectra are self-similar when normalised by their peaks (figure 2b, inset), the corresponding steepness-density spectra are not: smaller- T_p groups have relatively larger high-frequency tails (figure 10b), allowing them to reach a given limiting $\mathcal{S}_{\text{front}}(t_b)$ with a lower degree of wave group non-linearity.

Beyond wave scale, spectral bandwidth may also influence the limiting crest geometry, because it controls the duration of linear and non-linear interactions among the underlying components (McAllister et al., 2023). In the present comparisons, \mathcal{S}_p provides the clearest test of such a bandwidth effect as it is independent of bandwidth by definition. Within the limited range of γ tested here, however, the relation between $\mathcal{S}_{\text{front}}(t_b)$ and $\mathcal{S}_p(\chi_1)$ shows no measurable dependence on bandwidth (figure 9b). A broader range of γ would therefore be needed to assess this effect more fully.

The other robust result from figure 9 (right panels) is that $\mathcal{S}_{\text{front}}(t_b)$ exhibits a clear lower-bound threshold of approximately 0.2 across the unforced cases considered here. This threshold is not observed for \mathcal{S}_b or for any of the spectrally-informed wave-group steepness metrics. This highlights the importance of accounting for the front–rear asymmetry of the crest when defining a breaking-onset criterion, as $\mathcal{S}_{\text{front}}(t_b)$ does by construction.

Taken together, our results suggest that, among the five steepness metrics studied here, $\mathcal{S}_{\text{front}}(t_b)$ is the most reliable for representing the limiting local crest shape at incipient breaking in the absence of wind forcing and for defining a breaking-onset criterion through its relatively invariant lower-bound value.

| Independent variable | Proportional coefficient | Intercept | R^2 |
|----------------------|--------------------------|----------------------|-------|
| $\mathcal{S}_p(x_3)$ | 3.8 (± 1.30) | -0.94 (± 0.49) | 0.83 |
| $\mathcal{S}_s(x_3)$ | 3.2 (± 1.02) | -0.91 (± 0.45) | 0.84 |
| $\mathcal{S}_n(x_3)$ | 1.8 (± 0.49) | -0.83 (± 0.35) | 0.88 |

Table 2. Coefficients of the linear fits shown as red solid lines in figures 11(*b, e, h*). Fits are between $\mathcal{S}_{\text{front}}(t_b)$ and the different upstream wave-group steepness metrics for the strongest wind-forced breaking cases, $C_p/\overline{U_{10}} \approx 0.3$. These fitted relations are then used to normalise the data in figures 11(*c, f, i*).

4.2 Comparison in the presence of direct wind stress

4.2.1 Effect of wind on the steepness relationships

We now ask whether the relationships between locally-measured and spectrally-informed steepness we saw under unforced conditions (figure 6 in §4.1) also apply to breaking waves in the presence of co-flowing wind.

The left and middle columns from figure 11 present the same comparison as figure 9, but now for **BUBER** and **EURUS**. It should be noted that in assessing the wind effect, $\mathcal{S}_p(x_3)$, $\mathcal{S}_s(x_3)$, and $\mathcal{S}_n(x_3)$ can be treated as upstream independent variables because wind input only weakly modifies these metrics at x_3 under the present conditions (cf. figure 5). Of course, this approximation would be less appropriate if wind input substantially contaminated frequencies close to the upper limit of the integration band.

The results in figures 11(*a, d, and g*) reveal that \mathcal{S}_b remains approximately proportional to the three wave-group steepness metrics across the wind speeds considered. This suggests that, under the co-flowing wind conditions examined here, wind has only a weak influence on the local zero-crossing steepness at incipient breaking, a finding broadly consistent with the limited wind effect on maximum crest height reported by Touboul et al. (2006).

A clear wind influence is seen for $\mathcal{S}_{\text{front}}(t_b)$, however, as illustrated in figures 11*b, e, h*. Although the average threshold of $\mathcal{S}_{\text{front}}(t_b) \approx 0.2$ identified from the unforced cases still provides a useful breaking-onset reference (grey dashed lines), for a given wave-group steepness, wind-forced breaking appears to occur at smaller crest-front steepness. To make this reduction clearer, we fit the strongest wind-forced cases ($C_p/\overline{U_{10}} \approx 0.3$) in figures 11(*b, e, h*) using linear relations between $\mathcal{S}_{\text{front}}(t_b)$ and each wave-group steepness metric. These fits are shown as the red solid lines in figure 11, with the corresponding coefficients listed in table 2. The expected values given by the fits ($\widehat{\mathcal{S}}_{\text{front}, H}$) are then used to normalise all data in figures 11(*c, f, i*). In this way, $\mathcal{S}_{\text{front}}(t_b)/\widehat{\mathcal{S}}_{\text{front}, H} > 1$ indicates crest-front steepness larger than expected from the strongest-wind relation. These normalised results confirm that $\mathcal{S}_{\text{front}}(t_b)$ is reduced in the presence of wind and that the magnitude of this reduction scales positively with wind speed.

We find in figure 12(*a*) that relative to unforced cases, the wind-induced reduction in $\mathcal{S}_{\text{front}}(t_b)$ is associated with an increase in the crest-front distance $L'(t_b)$ at incipient breaking (see also figure 1*b* and equation (9)). This motivates us to examine the relative balance between the front (negative slope) and rear (positive slope) portions of the crest using the non-dimensional asymmetry parameter

$$\zeta = \frac{L'(t_b)}{L(t_b) - L'(t_b)}, \quad (13)$$

defined following Kjeldsen and Myrhaug (1979). Note that although this parameter was originally defined in the time domain, we apply it here in space. As shown in figure 12(*b*), wind-forced cases generally have larger ζ within the forward-leaning regime ($\zeta < 1$) compared to unforced cases, implying that the crest leans less forward and is more symmetric at incipient

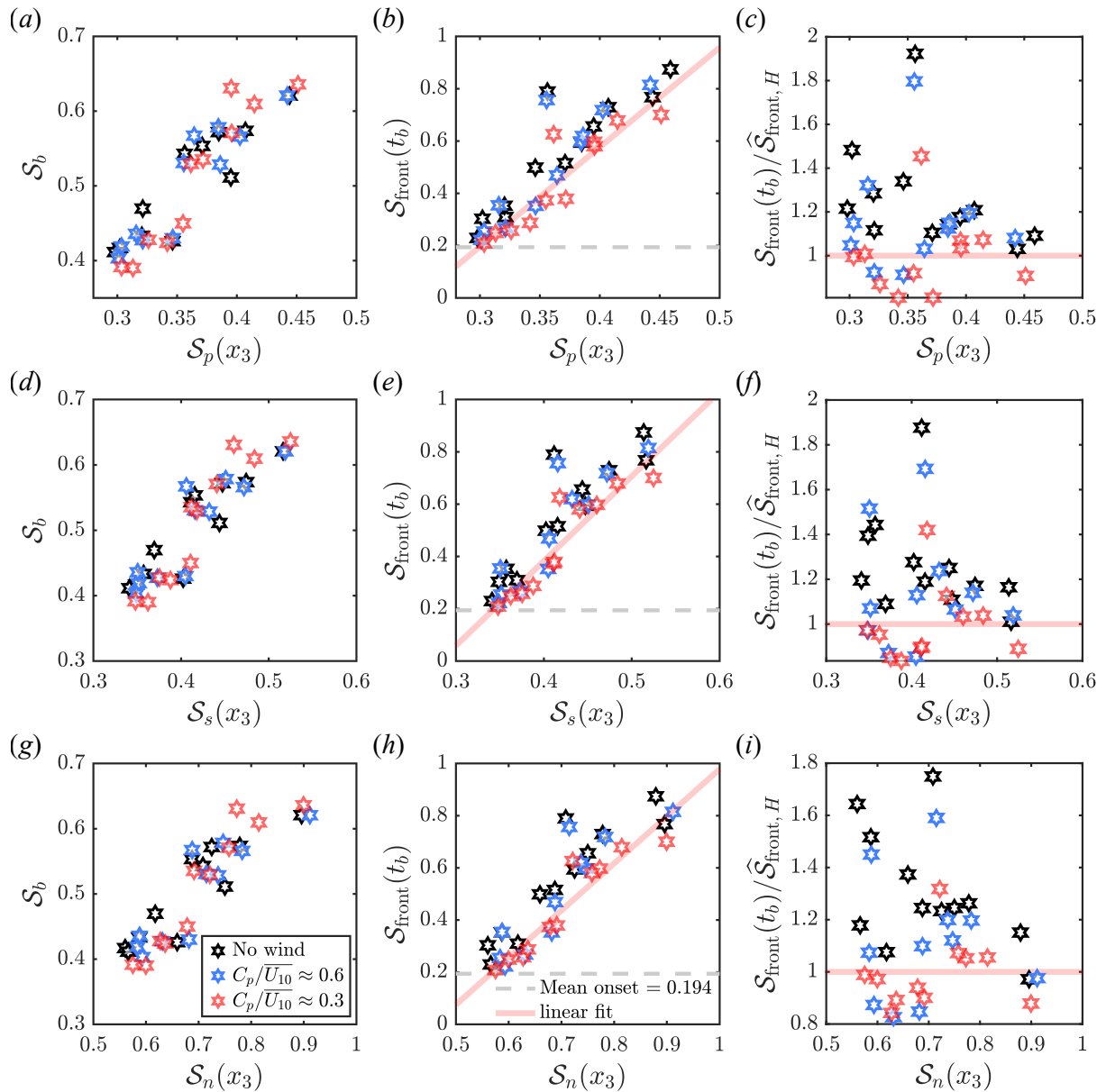


Figure 11. Comparisons of locally-measured crest steepness (\mathcal{S}_b and $\mathcal{S}_{\text{front}}(t_b)$) with spectrally-informed wave-group steepness ($\mathcal{S}_p(x_3)$, $\mathcal{S}_s(x_3)$, and $\mathcal{S}_n(x_3)$) for breaking cases from **BUBER** and **EURUS** under different wind speeds. Panels (a, d, g) show \mathcal{S}_b , and panels (b, e, h) show $\mathcal{S}_{\text{front}}(t_b)$. Grey dashed lines mark the average breaking-onset threshold identified in figure 9. Red solid lines are linear fits to the strongest wind-forced cases, with $C_p/\overline{U}_{10} \approx 0.3$. Panels (c, f, i) show $\mathcal{S}_{\text{front}}(t_b)$ normalised by these fits, so that the red lines correspond to unity.

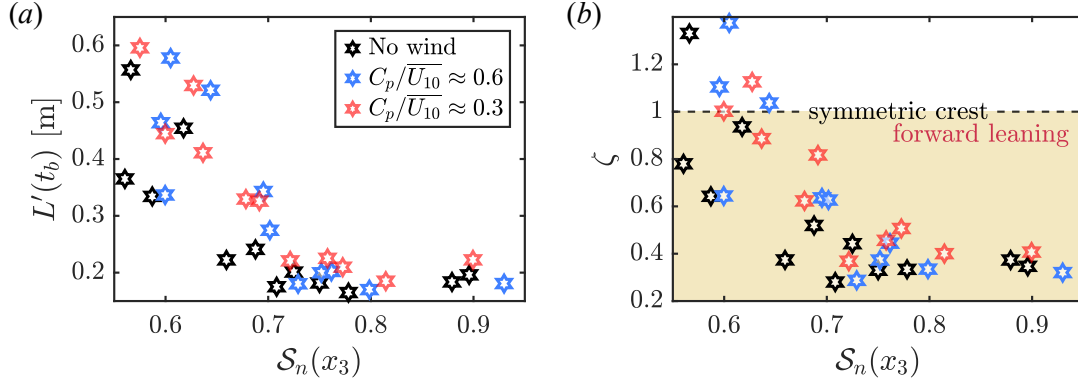


Figure 12. (a) Crest-front distance $L'(t_b)$ and (b) crest asymmetry parameter ζ (defined in equation (13)), plotted against $\mathcal{S}_n(x_3)$ for **BUBER** and **EURUS** breaking waves under varying co-flowing wind conditions. In (b), the dashed line indicates $\zeta = 1$ (corresponding to a symmetric crest) and the region shaded indicates the forward-leaning regime.

breaking. This wind-induced change in crest asymmetry appears strongest at lower $\mathcal{S}_n(x_3)$ and diminishes as $\mathcal{S}_n(x_3)$ increases. We interpret this to imply that a given level of wind forcing has a weaker relative effect on crest asymmetry for highly non-linear breaking wave groups compared to breaking wave groups with lower non-linearity. Further experiments with a greater range of wind forcing conditions would help to reinforce this interpretation.

4.2.2 Discussions on the wind effect

The wind-induced reduction in crest asymmetry and $\mathcal{S}_{\text{front}}(t_b)$ is a striking result. In deterministic focused wave groups, forward leaning is usually understood as a kinematic outcome of dispersive focusing: longer waves catch up with shorter waves, the crest narrows and slows, and kinetic energy is converted into potential energy as the crest steepens (Fedele et al., 2020). For strongly non-linear groups, breaking tends to occur during this slowdown phase, when the crest is most asymmetric. Our present results therefore suggest that this pathway to breaking is influenced by direct wind-forcing.

In addition, although the wave groups considered here were generated by the dispersive focusing (i.e. freely propagating components are expected to coalesce at a prescribed phase point), the actual breaking process is also affected by non-linear wave-wave interactions that occur during the relatively short wave group propagation duration before breaking occurs (Gibson and Swan, 2007). It is within this context that wind may affect the limiting crest geometry through several coupled mechanisms, some of which are directly supported by the present measurements and others inferred from previous studies:

- (i) As demonstrated in appendices A.2 and A.3, wind-induced drift currents impose disproportionate modulations on wave group dispersion between shorter and longer waves. Shorter components are more strongly advected by the near-surface (depth-dependent) current, reducing their relative intrinsic phase-speed difference with longer components. This can prolong the near-focusing state (i.e. the period over which the surface remains highly steepened but not necessarily in perfect phase alignment) and allow instabilities to develop over a longer interval, so that breaking need not wait for the crest to reach the same degree of forward leaning as in the unforced case.
- (ii) Wind also adds energy to the high-frequency part of the spectrum. Since breaking has long been associated with spectral saturation and the steepness of the high-frequency

tail (Phillips, 1985; Cao et al., 2023), this additional (free) short-wave content may help promote breaking. From appendix A.2 it is seen that in weakly non-linear groups, the wind-induced components tend to superimpose linearly onto the mechanically generated spectrum (figure 17). For highly non-linear wave groups their interaction with the underlying group becomes more complicated, including possible suppression or redistribution of energy to even shorter waves (Touboul et al., 2006; Gray, 2020).

- (iii) Albeit not directly measured here, aerodynamic sheltering (most commonly referred to as Jeffreys’ sheltering (Jeffreys, 1926)) cannot be ruled out as an additional mechanism by which wind may advance breaking. As discussed in §1.1 for sufficiently steep crests, airflow separation can generate pressure asymmetry between the windward and leeward faces (Iafrazi et al., 2019; Lee and Monty, 2020; Feddersen et al., 2023; Maleewong and Grimshaw, 2024; Tan et al., 2025). Such pressure perturbations can enhance particle velocities in the vicinity of the slowing wave crest and help satisfy a kinematic breaking condition earlier than in the unforced case (Babanin et al., 2010; Saket et al., 2017; Zou and Chen, 2017; Chen and Zou, 2022; Zhang et al., 2024). Evidence for this interpretation is provided by the numerical results of Boettger et al. (2024), who compared breaking waves of similar initial steepness with and without wind forcing. They found that wind led to earlier breaking inception and an approximately 35% increase in crest-tip kinetic energy relative to the unforced case before overturning. Similar observations were also reported by Xie (2017).
- (iv) Finally, the larger $\mathcal{S}_{\text{front}}(t_b)$ observed in unforced cases suggests that non-linear wave-wave interactions play a stronger role when wind is absent. In such cases, spectral energy around the largest crest can be redistributed into bound-wave components, increasing crest elevation, shortening the zero-crossing length scale, and producing a more asymmetric waveform (Johannessen and Swan, 2003; Gibson and Swan, 2007; Gray, 2020). Under wind forcing, by contrast, the dispersion modification, high-frequency input, and crest-airflow coupling mentioned above can lead to a relatively earlier occurrence of breaking, reducing the extent to which the crest must rely on non-linear amplification (and linear crest superposition) before breaking. In this sense, wind-wave interactions and non-linear wave-wave interactions act as competing processes and the balance between the two processes sets the effective limiting steepness at incipient breaking.

Whilst some of the mechanisms outlined above remain speculative and are not explicitly quantified here, the reduced limiting crest-front steepness under wind forcing can be reasonably interpreted as the combined effects of (i) wind-modified dispersion, (ii) enhanced high-frequency spectral content, and (iii) aerodynamic sheltering. Together, these effects suggest that breaking initiation is not set by geometry alone, whether measured spectrally or locally, but also requires energetic and kinematic considerations.

5 Summary of key insights and discussions

The present study examined the limiting geometry of unsteady breaking waves using three laboratory campaigns (**SIREN**, **BUBER** and **EURUS**) conducted in a unidirectional wind-wave flume. The experiments covered varying wave scales, a limited range of spectral bandwidths,

and co-flowing wind forcing. Combining in-situ wave-gauge measurements with surface reconstructions from a novel image-processing technique introduced in this study (namely SDBW-I), we have compared and contrasted spectrally-informed (wave-group) steepness, used as an upstream prognostic measure, with locally-measured steepness, used as a diagnostic measure of the crest geometry at incipient breaking.

Our first result concerns the spatial evolution of wave-group steepness. The three metrics considered, \mathcal{S}_p , \mathcal{S}_s and \mathcal{S}_n , remain approximately invariant when measured sufficiently far upstream of breaking. Closer to the breaking location, within approximately two dominant wavelengths upstream of x_b , \mathcal{S}_n systematically increases, demonstrating its stronger sensitivity to high-frequency spectral content during non-linear focusing. Whilst this makes \mathcal{S}_n useful for describing local wave-group (non-linear) evolution, caution is advised when using it as a predictive measure too close to the breaking location itself.

Our second result is that, in the absence of wind forcing, the local zero-crossing steepness \mathcal{S}_b scales quasi-linearly with upstream wave-group steepness, in line with earlier findings reported in the literature (e.g. Deike et al., 2016; Tian et al., 2010). Thus, when measured sufficiently far upstream, wave-group steepness can serve as a useful proxy for predicting \mathcal{S}_b at incipient breaking. This correspondence does not, however, extend in the same way to the crest-front steepness $\mathcal{S}_{\text{front}}(t_b)$. Instead, $\mathcal{S}_{\text{front}}(t_b)$ reveals a clear wave-scale dependence: larger-scale (i.e. higher T_p) wave groups require greater spectrally-informed steepness to reach the same limiting front-face geometry. This behaviour is consistent with their reduced high-frequency steepness density that can be important in triggering a breaking event.

The third result concerns the interpretation of steepness under wind forcing. Depending on the spectral cut-off, wave-group steepness \mathcal{S}_n can be strongly affected by high-frequency components generated explicitly by wind-forcing. The local steepness definition avoids this added complexity because it is measured directly from the crest geometry at incipient breaking, rather than inferred from a spectrally integrated quantity. For a given breaking event, wind has limited effect on \mathcal{S}_b , but it systematically reduces $\mathcal{S}_{\text{front}}(t_b)$ for a given wave-group steepness. This reduction is primarily associated with larger crest-front distances (L'), as opposed to a smaller incipient wave amplitude, and weaker forward leaning at incipient breaking (quantified by a crest asymmetry parameter, ζ). We interpret this as the combined effects of (i) wind-modified dispersion, (ii) enhanced high-frequency spectral content, and (iii) aerodynamic sheltering, which together can bring breaking forward before the crest reaches the more strongly forward-leaning form observed in unforced groups.

Taken together, these effects suggest that the presence of co-flowing wind, in a sense, reduces the extent to which wave breaking relies on non-linear energy transfer and focusing. More broadly these highlight that the initiation of breaking cannot be fully described by geometric considerations alone; energetic and kinematic processes must also be recognised.

Finally, we conclude that $\mathcal{S}_{\text{front}}(t_b)$ is the most useful steepness metric examined here for defining a breaking-onset criterion and characterising the limiting crest geometry at incipient breaking. It provides a consistent lower-bound threshold, with an average value of approximately $\mathcal{S}_{\text{front}}(t_b) \approx 0.2$, and naturally incorporates wind-induced changes in crest asymmetry. These attributes suggest that $\mathcal{S}_{\text{front}}(t_b)$ may serve as a useful local parameter for characterising the subsequent energetic and dynamic processes in breaking waves.

Acknowledgements

The authors gratefully acknowledge the experimental assistance given by the technicians, Mr. David Ruyter and Mr. Gary Austin, of the Hydrodynamics Laboratory at the Department of Civil and Environmental Engineering, Imperial College London.

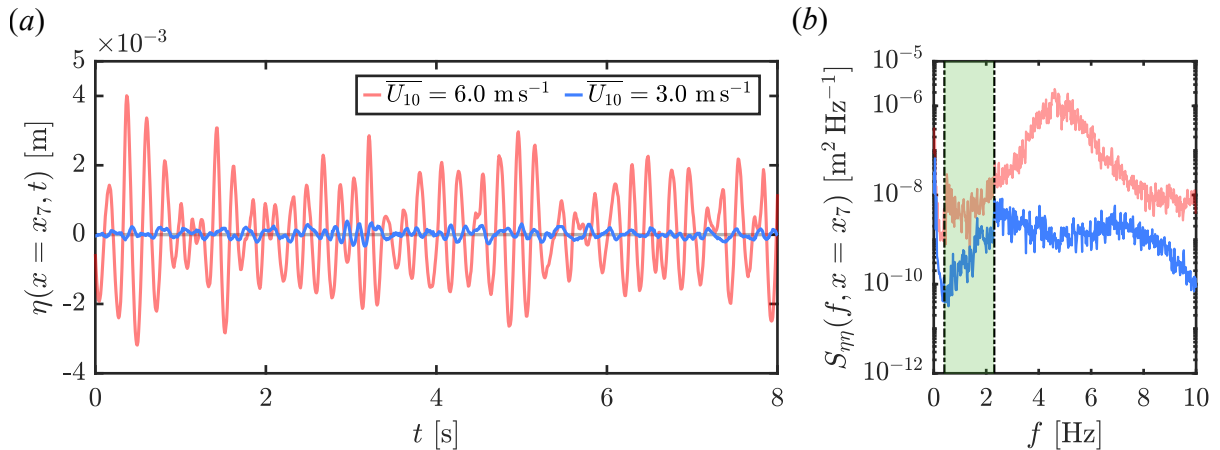


Figure 13. (a) Surface elevation time-series of wind-induced wave fields at the two wind speeds used in **EURUS**, upon reaching a statistically-stationary state. Measurements were taken at gauge 7 ($x = x_7$), the gauge closest to the focal/breaking location in **EURUS** (see also figure 3a). (b) Corresponding FFT variance density spectra calculated from 256 s surface elevation records. The region enclosed by the vertical dashed lines represents the frequency range of the target spectra used to generate paddle waves.

Funding

This work was supported by the Qingdao Postdoctoral Science Foundation (Grant No. QDBSH20250202010), the China Postdoctoral Science Foundation (Grant No. 2025M770858), and the Skempton PhD Scholarship awarded during R.C.'s doctoral studies at Imperial College London. The experimental campaigns reported herein, **SIREN**, **BUBER**, and **EURUS**, were funded by a NERC Standard Grant (Grant No. [NE/T000309/1](#)) awarded to A.H.C. in 2019.

Declaration of interests

The authors report no conflict of interest.

A Wind-forced non-breaking wave fields

While the wind conditions in **EURUS** were measured locally right above the breaking region (§2.3), the wind profile evolves along the fetch, leading to varying degrees of interactions with underlying wave fields. To place the breaking-wave results in context, it is therefore useful to first examine how co-flowing wind modifies non-breaking waves. The evolution of purely wind-induced wave fields and wind-forced, non-breaking focused wave groups has been examined in previous two-dimensional laboratory studies (Hara and Mei, 1991; Touboul et al., 2006; Grare et al., 2013; Gray, 2020; Shemer et al., 2020; Shemer and Singh, 2021; Kumar and Shemer, 2024). In this appendix, we report our own measurements of both cases and interpret them using mechanisms established in those studies, providing the physical context for the wind-forced breaking results discussed in the main text.

A.1 Purely wind-induced wave fields

Figure 13(a) shows examples of surface elevation time-series for wind-induced wave fields at statistically-steady state under $\bar{U}_{10} = 6.0$ and 3.0 m s^{-1} , measured near the breaking location in **EURUS**. The results demonstrate that background waves are generated by the overlying

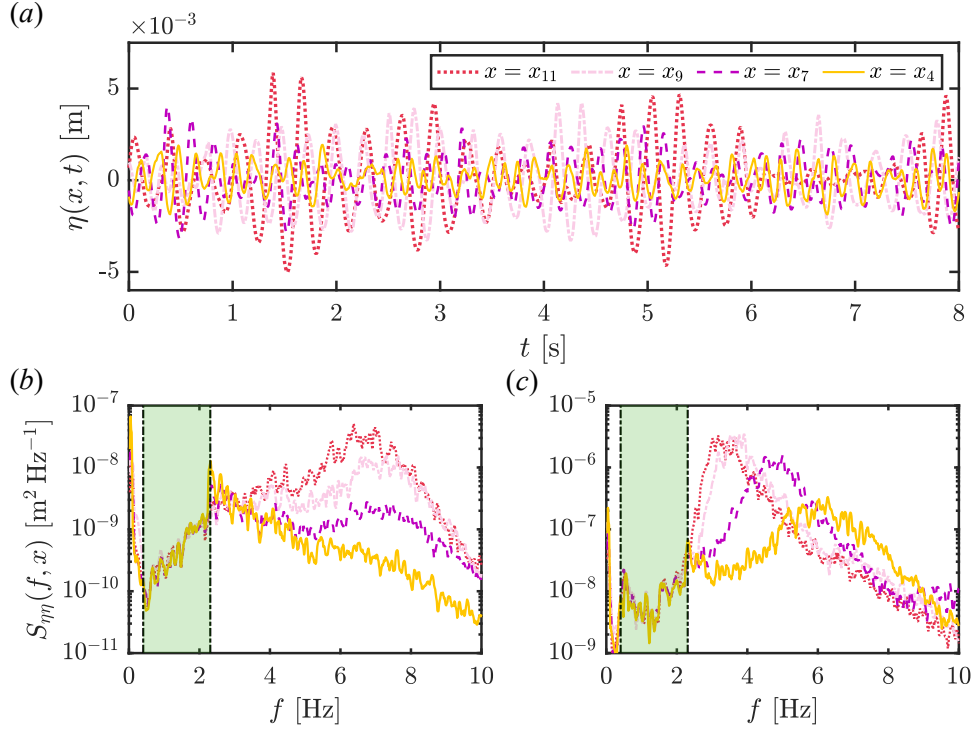


Figure 14. (a) Surface elevation time-series of a wind-induced, statistically stationary sea state at $\overline{U}_{10} = 6.0 \text{ m s}^{-1}$, recorded at different fetches: $x_4 = 6 \text{ m}$, $x_7 = 9.1 \text{ m}$, $x_9 = 13 \text{ m}$, and $x_{11} = 15.7 \text{ m}$ (see also figure 3a). Also shown are the FFT variance density spectra for (b) $\overline{U}_{10} = 3.0 \text{ m s}^{-1}$ and (c) $\overline{U}_{10} = 6.0 \text{ m s}^{-1}$, at these fetches. Again, the two black vertical dashed lines mark the lower and upper frequency limits of the designed paddle-wave spectrum, shown as shaded regions.

wind, but their development does not scale linearly with \overline{U}_{10} : at $\overline{U}_{10} = 6.0 \text{ m s}^{-1}$ a clear wave field develops, whereas at half this speed the waves are much weaker.

Figure 13(b) presents the corresponding FFT variance-density spectra, computed from 256 s surface-elevation records taken after more than 200 s of wind ramp-up and before paddle waves were generated. At this location, the stronger wind case ($\overline{U}_{10} = 6.0 \text{ m s}^{-1}$) shows increased spectral energy across the full frequency range, with a distinct peak near $f \approx 5 \text{ Hz}$, beyond the designed paddle-wave spectrum. No comparable peak is observed at the lower wind speed.

To examine the fetch dependence at these wind speeds, we plot in figure 14(a) the surface elevation time-series recorded at several gauges under $\overline{U}_{10} = 6.0 \text{ m s}^{-1}$. The results show a consistent increase in wave amplitude (and scale) with fetch, and the spectra in figures 14(b, c) show how this development depends on wind speed. For both wind speeds, spectral growth occurs mainly beyond the upper frequency limit of the target paddle-wave spectrum in the higher frequency band. At $\overline{U}_{10} = 3.0 \text{ m s}^{-1}$, no distinct peak forms until the most downstream location shown, x_{11} , where a maximum appears at $f \approx 6.8 \text{ Hz}$. By contrast, at $\overline{U}_{10} = 6.0 \text{ m s}^{-1}$, a high frequency peak is present throughout; with increasing fetch, this peak both amplifies and shifts progressively towards lower frequencies.

Overall, the above observations highlight the role of overlying wind in amplifying high-frequency spectral energy in wind-induced wave fields, with stronger wind and longer fetch promoting both continued spectral growth and redistribution towards lower frequencies (longer waves). These findings agree well with previous studies of purely wind-induced sea states (e.g. Hara and Mei, 1991; Grare et al., 2013; Kumar and Shemer, 2024; Do et al., 2024).

A.2 Evolution of non-breaking focused wave groups in the presence of wind forcing

Having gained insight into the behaviour of purely wind-induced wave fields, we now examine how co-flowing wind modifies weakly non-linear, non-breaking focused wave groups. To minimise the role of intrinsic non-linearity, we focus on case G2Tp13A040, which had the smallest A in **BUBER** and **EURUS**. Unforced and wind-forced runs are compared at the same fetch distances, with the prescribed x_f and t_f kept unchanged. As mentioned earlier, the wind was allowed to blow for 8 minutes such that a statistically-steady background wave field was established before the focused wave group was generated.

The surface elevation time-series, $\eta(t)$, are shown in the left panels of figure 15, where (a , c , e , and g) correspond to measurements upstream of the focal point x_f and (i) is downstream. Near the wave generation paddle (a , c), differences between wind and no-wind conditions are negligible, as the fetch is too short for substantial wind-wave interaction and the airflow itself is still developing. Further downstream (e , g , and i), deviations become apparent: $\eta(t)$ of wind-forced wave groups is shifted forward in time, suggesting faster propagation, with the shift increasing with wind speed. The crests also appear more disturbed, and slightly higher, under wind forcing.

Together these observations imply that the wind-forced groups no longer focus at the same time or location as the corresponding unforced groups, even though no wave gauge was placed exactly at the focal point. Indeed, Gray (2020) demonstrated that under wind action, frequency components, particularly at higher frequencies, lose phase coherence at the target focal point, thereby displacing the point of maximum symmetry further downstream. This is fully consistent with our observations, for which both the actual focal location and the incipient breaking point shifted downstream while the prescribed x_f remained unchanged.

This behaviour can be interpreted in terms of wind-modified dispersion. Under wind forcing, a thin shear layer forms near the free surface, with a thickness of order $\mathcal{O}(1 \text{ mm} - 1 \text{ cm})$ (Banner and Phillips, 1974; Tian and Choi, 2013; Zou and Chen, 2017). Within this layer, the wind-induced drift current has a depth-dependent velocity profile (Zou and Chen, 2017; Chen and Zou, 2022), from which Doppler-like modifications to the phase velocity of each spectral component arise. In a linear manner the modified phase velocity for a spectral component can be approximated according to Cummins and Swan (1993) as:

$$c_{i,\text{mod}} = \underbrace{\sqrt{\frac{g}{k_i} \tanh k_i d}}_{c_i} + \underbrace{\left[u_{\text{drift}}(x)|_{z=\eta} - \frac{\partial u_{\text{drift}}(x, z)}{\partial z} \frac{\tanh k_i d}{k_i} \right]}_{\text{wind-induced advection}}, \quad (14)$$

where c_i and $c_{i,\text{mod}}$ are the intrinsic and wind-modified phase velocities, $u_{\text{drift}}(x)|_{z=\eta}$ is the surface drift velocity at location x , and $\partial u_{\text{drift}}(x, z)/\partial z$ is the vertical shear. The resulting phase velocity change modifies the frequency relative to its intrinsic, wind-free value, f_i , such that

$$f_{i,\text{mod}} = \Gamma_i f_i, \quad (15)$$

with the modulation factor given by:

$$\Gamma_i = 1 + u_{\text{drift}}(x)|_{z=\eta} \sqrt{\frac{k_i}{g} \coth(k_i d)} - \frac{\partial u_{\text{drift}}(x, z)}{\partial z} \sqrt{\frac{\tanh(k_i d)}{k_i g}} \quad (16)$$

Since we did not explicitly measure the surface drift velocity nor its vertical shear profile,

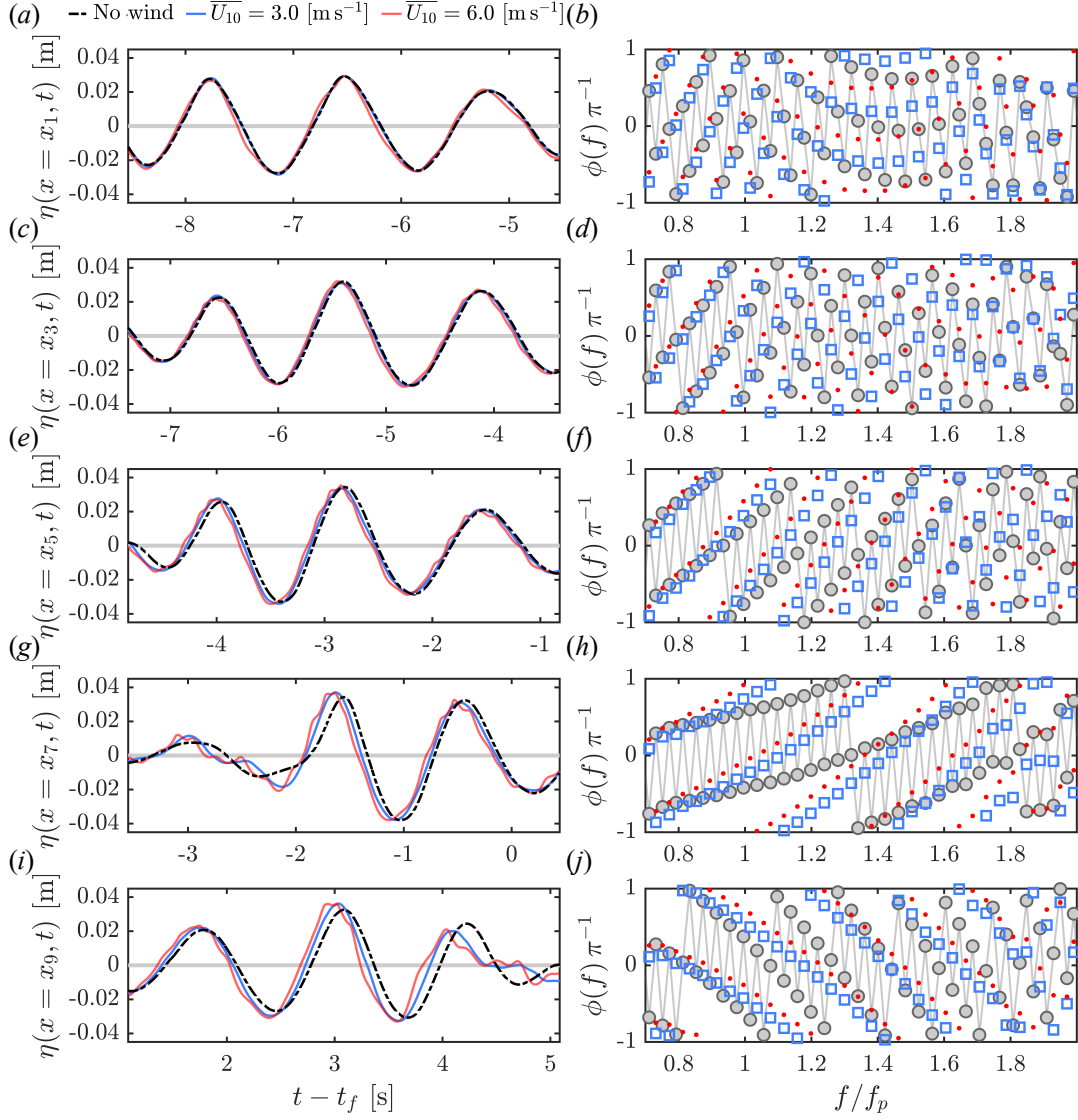


Figure 15. Surface elevation time-series $\eta(x, t)$ (left panels) and normalised FFT phase angles $\phi(f) \pi^{-1}$ (right panels) for G2Tp13A040 from **BUBER** (no wind) and **EURUS** (with wind). Records were taken at (a, b) $x_1 = 2.4$ m, (c, d) $x_3 = 4.5$ m, (e, f) $x_5 = 7.0$ m, (g, h) $x_7 = 9.1$ m, closest to the focal/breaking location, and (i, j) $x_9 = 13$ m (see also figure 3a). All cases had the same prescribed focal location x_f and time t_f .

approximation based on previous studies is executed in estimating $c_{i,\text{mod}}$ and $f_{i,\text{mod}}$ using the equations above. We follow [Zou and Chen \(2017\)](#) and [Chen and Zou \(2022\)](#) and consider the drift profile at a given x in a surface-following frame (i.e. the depth z is measured relative to the instantaneous surface elevation), such that:

$$u_{\text{drift}}(z) = u_{\text{drift}}|_{z=\eta} \cdot e^{(z-\eta)/\delta^*}, \quad \text{for } z \in [\eta - d, \eta], \quad (17)$$

where δ^* is the characteristic (e -folding) thickness of the drift layer for which the velocity decays exponentially with depth and attenuates to a negligible level over a depth of order $\pi\delta^*$ beneath the surface ([Zou and Chen, 2017](#)). The corresponding vertical shear is:

$$\frac{\partial u_{\text{drift}}(z)}{\partial z} = \frac{u_{\text{drift}}|_{z=\eta}}{\delta^*} \cdot e^{(z-\eta)/\delta^*}. \quad (18)$$

To obtain a representative velocity gradient beneath the surface, we define a characteristic shear as the depth-averaged value of equation (18) over an upper layer of depth equal to the wavelength λ , i.e. $z \in [\eta - \lambda, \eta]$. This is motivated by the fact that current shear modifies wave phase velocity mainly through the velocity profile over a depth comparable to the wavelength. Accordingly,

$$\left\langle \frac{\partial u_{\text{drift}}}{\partial z} \right\rangle = \frac{1}{\lambda} \int_{\eta-\lambda}^{\eta} \frac{u_{\text{drift}}|_{z=\eta}}{\delta^*} \cdot e^{(z-\eta)/\delta^*} dz \quad (19)$$

$$= \frac{u_{\text{drift}}|_{z=\eta}}{\lambda\delta^*} \int_{-\lambda/\delta^*}^0 e^{\xi} \cdot \delta^* d\xi \quad (\text{by letting } \xi = \frac{z-\eta}{\delta^*}) \quad (20)$$

$$= \frac{u_{\text{drift}}|_{z=\eta}}{\lambda} \left(1 - e^{-\lambda/\delta^*}\right). \quad (21)$$

When $\lambda > d$, λ is replaced by d to satisfy the impermeable bed condition. The thickness of the drift layer is taken as $\delta^* = 0.01$ m for both wind conditions, consistent with [Zou and Chen \(2017\)](#), whose measurements were made under comparable wind speeds. The surface drift velocity is commonly scaled with the wind friction velocity u_* , and following [Grare et al. \(2013\)](#), we adopt $u_{\text{drift}}|_{z=\eta} = 0.3u_*$. From the airflow measurements at probe 2, $u_* = 0.07$ m s⁻¹ and $u_* = 0.21$ m s⁻¹ correspond to surface drift velocities of $u_{\text{drift}}|_{z=\eta} = 0.021$ m s⁻¹ and $u_{\text{drift}}|_{z=\eta} = 0.063$ m s⁻¹ at $\overline{U}_{10} = 3.0$ m s⁻¹ and $\overline{U}_{10} = 6.0$ m s⁻¹, respectively. These estimates are consistent with previous reports that $u_{\text{drift}}|_{z=\eta} \sim \mathcal{O}(1\% \overline{U}_{10})$ ([Tian and Choi, 2013](#)). Substituting these values and δ^* into equations (21) and (16), together with equations (14) and (15), provides a first-order estimate of wind-induced modulations of the dispersion relation for small amplitude waves.

The results are presented in figure 16, where panel (a) shows how wind alters the intrinsic frequency of individual components and (b) shows the corresponding change in phase speed. We confirm that wind has a greater impact on higher-frequency components through more effective advection. This arises because the wind-induced shear is confined to a shallow layer beneath the free surface, from which only shorter waves can feel its full effect. In this sense, the finite thickness of the drift layer sets an approximate upper wavelength beyond which waves are only weakly modified ([Banner and Phillips, 1974](#); [Tian and Choi, 2013](#); [Chen and Zou, 2022](#); [Martin-Blanco et al., 2026](#)).

To examine this interpretation, we compare the FFT phase angles of unforced and wind-forced wave groups in the right-hand panels (b, d, f, h, and j) of figure 15. For clarity, only the spectral energy-containing range $0.6 \leq f/f_p \leq 2$ is shown (c.f. figure 2b). It is clear from these plots that while lower-frequency components appear visually in phase, positive phase offsets are

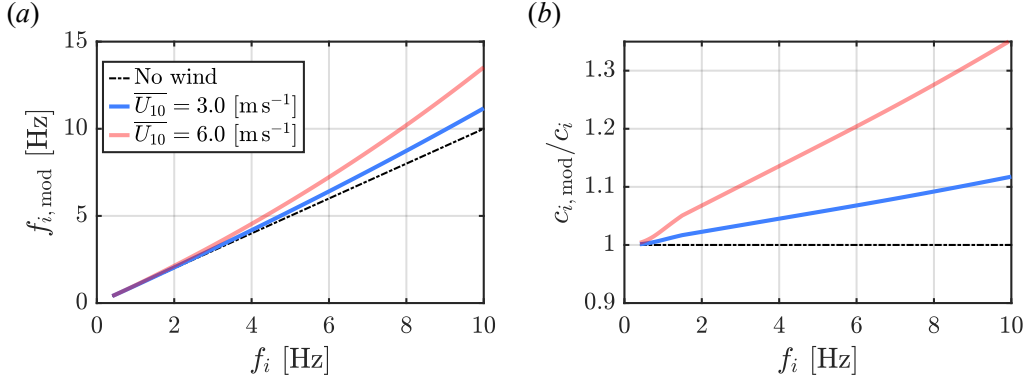


Figure 16. Wind-induced modulation of the dispersion relation under different wind speeds. (a) Wind-modulated frequency $f_{i,\text{mod}}$ versus the intrinsic frequency f_i . (b) Ratio of wind-modulated phase speed $c_{i,\text{mod}}$ to the intrinsic phase velocity c_i , plotted as a function of f_i .

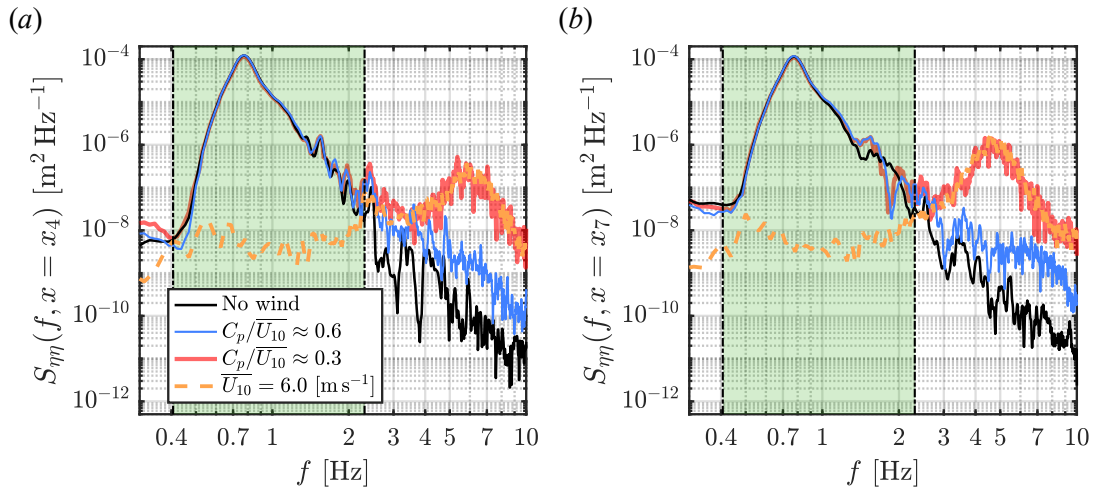


Figure 17. FFT variance density spectra for G2Tp13A040 from **BUBER** (no wind) and **EURUS** (with wind), recorded at (a) $x_4 = 6.0$ m and (b) $x_7 = 9.1$ m. Orange lines show spectra of purely wind-induced waves under the strongest wind speed, $\bar{U}_{10} = 6.0$ m s $^{-1}$. Vertical dashed lines mark the active frequency range of wave-generation paddle, corresponding to the target spectrum. The x -axis is plotted on a logarithmic scale to highlight wind effects.

identified at higher frequencies under wind forcing. These offsets grow with increasing fetch and wind speed.

The above phase behaviour supports the argument that higher-frequency components are more readily advected by co-flowing wind, while lower-frequency components, being intrinsically faster, are less affected. The resulting reduction in phase-speed contrast between short and long components slows their phase convergence, so that the wave group requires a longer time and distance to reach full focusing. This is also consistent with the experimental observations of [Touboul et al. \(2006\)](#) and [Gray \(2020\)](#), who found that focused groups preserve coherence over extended durations when exposed to wind.

From an energetic perspective, we compare variance density spectra for G2Tp13A040 at two fetches and under different wind speeds in figure 17. Within the target frequency range, wind has little influence at x_4 (close to the first wind probe, panel a), but by x_7 changes appear at higher frequencies, about $f > 1.3$ Hz (panel b). The dominant wind effect remains beyond the designed spectral limit, where spectral energy increases substantially with wind speed. In both panels, the spectrum of wind-induced waves at $\bar{U}_{10} = 6.0$ m s $^{-1}$ is also shown; its high-frequency tail accounts for most of the spectral energy in this range of the combined wind-wave

spectra. This partly echoes the conclusion of [Lee and Monty \(2020\)](#): direct wind forcing does not necessarily strengthen higher-order non-linear wave–wave interactions, and the additional growth observed here arises primarily from (linear) wind–wave interactions.

A.3 Summary of the wind effect on unsteady, non-breaking wave groups

The experimental results presented in this appendix (A) reveal several effects of co-flowing wind on weakly non-linear, unsteady wave groups under non-breaking conditions, consistent with the findings of [Touboul et al. \(2006\)](#), [Gray \(2020\)](#), and [Chen and Zou \(2022\)](#). The main physical mechanisms are summarised as follows:

- The presence of overlying wind amplifies spectral energy at the higher-frequency band, introducing additional short waves whose energy is dominated linearly by purely wind-induced components. This appears as increased surface disturbance on the wave-group profile.
- Wind-induced drift currents modulate wave-group dispersion, causing the groups to propagate faster and focus further downstream than their equivalent wave groups when no wind is present. These effects become more pronounced at higher wind speeds.
- The apparently contrasting observations of a forward time shift (suggesting shorter time to focus) and a downstream shift of the focal location (suggesting longer distance to focus) can be reconciled by the inconsistent influence of drift currents across spectral components. Shorter waves are more strongly advected than longer waves ([Banner and Phillips, 1974](#); [Gray, 2020](#)), reducing their relative phase-speed difference and delaying their phase alignment. As a result, the group can arrive earlier at a given gauge while still requiring a longer distance for a focused event to form.
- Although the added spectral energy near and above the upper frequency limit of the designed spectrum is relatively small, this band is important for breaking initiation through spectral saturation ([Phillips, 1985](#); [Kway et al., 1998](#)). This motivates our analysis in the main text of how wind modifies the steepness at which breaking occurs.

References

- Babanin, A. V., Chalikov, D., Young, I. R., and Savelyev, I. (2010). Numerical and laboratory investigation of breaking of steep two-dimensional waves in deep water. *Journal of Fluid Mechanics*, 644:433–463.
- Babanin, A. V., McConochie, J., and Chalikov, D. (2018). Winds near the Surface of Waves, Observations and Modelling. *Journal of Physical Oceanography*, pages 1079–1088.
- Baldock, T. E., Swan, C., and Taylor, P. H. (1996). A laboratory study of nonlinear surface waves on water. *Philosophical Transactions of the Royal Society of London. Series A: Mathematical, Physical and Engineering Sciences*, 354(1707):649–676.
- Banner, M. L., Barthelemy, X., Fedele, F., Allis, M., Benetazzo, A., Dias, F., and Peirson, W. L. (2014). Linking Reduced Breaking Crest Speeds to Unsteady Nonlinear Water Wave Group Behavior. *Physical Review Letters*, 112(11):114502.
- Banner, M. L. and Peirson, W. L. (2007). Wave breaking onset and strength for two-dimensional deep-water wave groups. *Journal of Fluid Mechanics*, 585:93–115.

- Banner, M. L. and Phillips, O. M. (1974). On the incipient breaking of small scale waves. *Journal of Fluid Mechanics*, 65(04):647–656.
- Barthelemy, X., Banner, M. L., Peirson, W. L., Fedele, F., Allis, M., and Dias, F. (2018). On a unified breaking onset threshold for gravity waves in deep and intermediate depth water. *Journal of Fluid Mechanics*, 841:463–488.
- Boettger, D. G., Keating, S. R., Banner, M. L., Morison, R. P., and Barthélémy, X. (2023). An energetic signature for breaking inception in surface gravity waves. *Journal of Fluid Mechanics*, 959:A33.
- Boettger, D. G., Keating, S. R., Banner, M. L., Morison, R. P., and Barthélémy, X. (2024). Energetic inception of breaking in surface gravity waves under wind forcing. *Physical Review Fluids*, 9(5):8–12.
- Buckley, M. P., Horstmann, J., Savelyev, I., and Carpenter, J. R. (2025). Direct observations of airflow separation over ocean surface waves. *Nature Communications*, 16.
- Buckley, M. P. and Veron, F. (2016). Structure of the Airflow above Surface Waves. *Journal of Physical Oceanography*, 46(5):1377–1397.
- Callaghan, A. H., Deane, G. B., and Stokes, M. D. (2013). Two Regimes of Laboratory Whitecap Foam Decay: Bubble-Plume Controlled and Surfactant Stabilized. *Journal of Physical Oceanography*, 43(6):1114–1126.
- Cao, R. (2024). *The dynamics, energetics, and air entrainment of unsteady breaking waves in the absence and presence of direct wind stress*. PhD thesis, Imperial College London, London, UK.
- Cao, R., Padilla, E., and Callaghan, A. (2023). The influence of bandwidth on the energetics of intermediate to deep water laboratory breaking waves. *Journal of Fluid Mechanics*, 971:A11.
- Cao, R., Padilla, E. M., Chen, X., and Callaghan, A. H. (2026). A representative underlying scale for spectrally resolved energy dissipation in surface breaking waves. *Journal of Geophysical Research: Oceans*, 131:e2025JC023904.
- Cao, R., Padilla, E. M., Fang, Y., and Callaghan, A. H. (2025). Identification of the free surface for unidirectional nonbreaking water waves from side-view digital images. *IEEE Journal of Oceanic Engineering*, 50(1):204–212.
- Chalikov, D. and Rainchik, S. (2011). Coupled numerical modelling of wind and waves and the theory of the wave boundary layer. *Boundary-Layer Meteorology*, 138:1–41.
- Chen, H. and Zou, Q. (2022). Geometry of deep and intermediate water breaking waves influenced by wind speed and direction. *Physics of Fluids*, 34(8).
- Cui, T., He, G., Jiang, M., Wang, W., Yuan, L., Han, D., Kamath, A., and Bihs, H. (2022). Large eddy simulation of focused breaking waves with different wave steepness. *Ocean Modelling*, 179(March):102122.
- Cummins, I. and Swan, C. (1993). *Non-Linear Wave Current Interactions*, pages 35–51. Springer Netherlands, Dordrecht.
- De Vita, F., Verzicco, R., and Iafrati, A. (2018). Breaking of modulated wave groups: Kinematics and energy dissipation processes. *Journal of Fluid Mechanics*, 855:267–298.

- Deane, G. B. and Stokes, M. D. (2002). Scale dependence of bubble creation mechanisms in breaking waves. *Nature*, 418(6900):839–844.
- Deane, G. B., Stokes, M. D., and Callaghan, A. H. (2016). The Saturation of Fluid Turbulence in Breaking Laboratory Waves and Implications for Whitecaps. *Journal of Physical Oceanography*, 46(3):975–992.
- Deike, L. (2022). Mass Transfer at the Ocean–Atmosphere Interface: The Role of Wave Breaking, Droplets, and Bubbles. *Annual Review of Fluid Mechanics*, 54(1):191–224.
- Deike, L., Melville, W. K., and Popinet, S. (2016). Air entrainment and bubble statistics in breaking waves. *Journal of Fluid Mechanics*, 801:91–129.
- Deike, L., Popinet, S., and Melville, W. K. (2015). Capillary effects on wave breaking. *Journal of Fluid Mechanics*, 769:541–569.
- Derakhti, M. and Kirby, J. T. (2014). Bubble entrainment and liquid–bubble interaction under unsteady breaking waves. *Journal of Fluid Mechanics*, 761:464–506.
- Derakhti, M. and Kirby, J. T. (2016). Breaking-onset, energy and momentum flux in unsteady focused wave packets. *Journal of Fluid Mechanics*, 790:553–581.
- Derakhti, M., Kirby, J. T., Banner, M. L., Grilli, S. T., and Thomson, J. (2020). A Unified Breaking Onset Criterion for Surface Gravity Water Waves in Arbitrary Depth. *Journal of Geophysical Research: Oceans*, 125(7):1–28.
- Do, J., Wang, B., and Chang, K. A. (2024). Turbulence over young wind waves dominated by capillaries and micro-breakers. *Journal of Fluid Mechanics*, 985:A22.
- Drazen, D. A., Melville, W. K., and Lenain, L. (2008). Inertial scaling of dissipation in unsteady breaking waves. *Journal of Fluid Mechanics*, 611:307–332.
- Duncan, J. (2001). Spilling breakers. *Annual Review of Fluid Mechanics*, 33(Volume 33, 2001):519–547.
- Erinin, M., Liu, X., Wang, S., and Duncan, J. (2023). Plunging breakers. Part 1. Analysis of an ensemble of wave profiles. *Journal of Fluid Mechanics*, 967:A35.
- Fedderson, F., Fincham, A. M., Brodie, K. L., Young, A. P., Spydell, M., Grimes, D. J., Pieszka, M., and Hanson, K. (2023). Cross-shore wind-induced changes to field-scale overturning wave shape. *Journal of Fluid Mechanics*, 958:A4.
- Fedele, F., Banner, M. L., and Barthelemy, X. (2020). Crest speeds of unsteady surface water waves. *Journal of Fluid Mechanics*, 899:A5.
- Gibson, R. and Swan, C. (2007). The evolution of large ocean waves: the role of local and rapid spectral changes. *Proceedings of the Royal Society A: Mathematical, Physical and Engineering Sciences*, 463:21–48.
- Grare, L., Peirson, W. L., Branger, H., Walker, J. W., Giovanangeli, J. P., and Makin, V. (2013). Growth and dissipation of wind-forced, deep-water waves. *Journal of Fluid Mechanics*, 722:5–50.
- Gray, A. (2020). *Extreme waves under significant wind stress*. PhD thesis, Imperial College London, London, UK.

- Hanson, J. L. and Phillips, O. M. (1999). Wind Sea Growth and Dissipation in the Open Ocean. *Journal of Physical Oceanography*, 29(8):1633–1648.
- Hara, T. and Mei, C. C. (1991). Frequency downshift in narrowbanded surface waves under the influence of wind. *Journal of Fluid Mechanics*, 230:429–477.
- Hogan, L., Zappa, C. J., Cifuentes-Lorenzen, A., Edson, J. B., O’Donnell, J., and Ullman, D. S. (2025). Observations of breaking wave dissipation and their relationship to atmosphere-ocean energy transfer. *Journal of Geophysical Research: Oceans*, 130.
- Hulin, F., Prevosto, M., Tassin, A., François Filipot, J., Jacques, N., and Grilli, S. (2025). Breaking onset and breaking strength of focused wave packets: Linear prediction model and nonlinear numerical simulations. *Coastal Engineering*, 197:104660.
- Iafrafi, A., De Vita, F., and Verzicco, R. (2019). Effects of the wind on the breaking of modulated wave trains. *European Journal of Mechanics - B/Fluids*, 73:6–23.
- Jeffreys, H. (1926). On the formation of water waves by wind (second paper). *Proceedings of The Royal Society A*, 110(754):241–247.
- Johannessen, T. and Swan, C. (2001). A laboratory study of the focusing of transient and directionally spread surface water waves. *Proceedings of the Royal Society of London. Series A: Mathematical, Physical and Engineering Sciences*, 457(2008):971–1006.
- Johannessen, T. B. and Swan, C. (2003). On the nonlinear dynamics of wave groups produced by the focusing of surface-water waves. *Proceedings of the Royal Society A: Mathematical, Physical and Engineering Sciences*, 459(2032):1021–1052.
- Kjeldsen, S. and Myrhaug, D. (1979). Breaking waves in deep water and resulting wave forces. volume All Days of *OTC Offshore Technology Conference*, pages OTC-3646–MS.
- Knobler, S., Winiarska, E., Babanin, A., and Liberzon, D. (2022). Wave breaking probabilities under wind forcing in open sea and laboratory. *Physics of Fluids*, 34.
- Kristoffersen, J. C., Bredmose, H., Georgakis, C. T., Branger, H., and Luneau, C. (2021). Experimental study of the effect of wind above irregular waves on the wave-induced load statistics. *Coastal Engineering*, 168(June).
- Kumar, K. and Shemer, L. (2024). Laboratory study of the effect of mean water current on the evolution of young wind waves. *Journal of Fluid Mechanics*, 996:A21.
- Kway, J. H., Loh, Y.-S., and Chan, E.-S. (1998). Laboratory study of deep-water breaking waves. *Ocean Engineering*, 25:657–676.
- Lee, J. H. and Monty, J. P. (2020). On the interaction between wind stress and waves: Wave growth and statistical properties of large waves. *Journal of Physical Oceanography*, 50(2):383–397.
- Lee, J. H., Monty, J. P., Elsnab, J., Toffoli, A., Babanin, A. V., and Alberello, A. (2017). Estimation of Kinetic Energy Dissipation from Breaking Waves in the Wave Crest Region. *Journal of Physical Oceanography*, 47(5):1145–1150.
- Maleewong, M. and Grimshaw, R. (2024). Evolution of wind-induced wave groups in water of finite depth. *Journal of Fluid Mechanics*, 985.

- Martin-Blanco, C., Scapin, N., Wu, J., Popinet, S., Farrar, J. T., Chapron, B., and Deike, L. (2026). Kinematics of gravity–capillary waves above an evolving underwater current. *Journal of Fluid Mechanics*, 1035:A5.
- McAllister, M. L., Draycott, S., Calvert, R., Davey, T., Dias, F., and van den Bremer, T. S. (2024). Three-dimensional wave breaking. *Nature*, 633(8030):601–607.
- McAllister, M. L., Pizzo, N., Draycott, S., and Van Den Bremer, T. S. (2023). The influence of spectral bandwidth and shape on deep-water wave breaking onset. *Journal of Fluid Mechanics*, 974:1–27.
- Melville, W. K. (1994). Energy dissipation by breaking waves. *Journal of Physical Oceanography*, 24:2041–2049.
- Melville, W. K. (1996). The Role of Surface-Wave Breaking in Air-Sea Interaction. *Annual Review of Fluid Mechanics*, 28(1):279–321.
- Miles, J. W. (1957). On the generation of surface waves by shear flows. *Journal of Fluid Mechanics*, 3(2):185–204.
- Na, B., Chang, K.-a., and Lim, H.-j. (2020). Flow kinematics and air entrainment under laboratory spilling breaking waves. *Journal of Fluid Mechanics*, 882:A15.
- Oh, S.-H., Mizutani, N., Suh, K.-D., and Hashimoto, N. (2005). Experimental investigation of breaking criteria of deepwater wind waves under strong wind action. *Applied Ocean Research*, 27(4-5):235–250.
- Olfateh, M., Ware, P., Callaghan, D. P., Nielsen, P., and Baldock, T. E. (2017). Momentum transfer under laboratory wind waves. *Coastal Engineering*, 121(April 2016):255–264.
- Padilla, E. M., Cao, R., and Callaghan, A. H. (2023). Spatial interpolation of wave fields based on limited spatial measurements. *IEEE Journal of Oceanic Engineering*, 48:1226–1235.
- Perlin, M., Choi, W., and Tian, Z. (2013). Breaking Waves in Deep and Intermediate Waters. *Annual Review of Fluid Mechanics*, 45(1):115–145.
- Phillips, O. M. (1985). Spectral and statistical properties of the equilibrium range in wind-generated gravity waves. *Journal of Fluid Mechanics*, 156:505.
- Pizzo, N., Murray, E., Smith, D. L., and Lenain, L. (2021). The role of bandwidth in setting the breaking slope threshold of deep-water focusing wave packets. *Physics of Fluids*, 33(11):111706.
- Rapp, R. J. and Melville, W. K. (1990). Laboratory Measurements of Deep-Water Breaking Waves. *Philosophical Transactions of the Royal Society A: Mathematical, Physical and Engineering Sciences*, 331(1622):735–800.
- Romero, L. (2019). Distribution of surface wave breaking fronts. *Geophysical Research Letters*, 46:10463–10474.
- Saket, A., Peirson, W. L., Banner, M. L., Barthelemy, X., and Allis, M. J. (2017). On the threshold for wave breaking of two-dimensional deep water wave groups in the absence and presence of wind. *Journal of Fluid Mechanics*, 811:642–658.
- Scapin, N., Wu, J., Farrar, J. T., Chapron, B., Popinet, S., and Deike, L. (2025). Momentum fluxes in wind-forced breaking waves. *Journal of Fluid Mechanics*, 1009.

- She, K., Greated, C. A., and Easson, W. J. (1994). Experimental Study of Three-Dimensional Wave Breaking. *Journal of Waterway, Port, Coastal, and Ocean Engineering*, 120(1):20–36.
- Shemer, L. and Singh, S. K. (2021). Spatially evolving regular water wave under the action of steady wind forcing. *Physical Review Fluids*, 6(3):34802.
- Shemer, L., Singh, S. K., and Chernyshova, A. (2020). Spatial evolution of young wind waves: numerical modelling verified by experiments. *Journal of Fluid Mechanics*, 901:A22.
- Sinnis, J. T., Grare, L., Lenain, L., and Pizzo, N. (2021). Laboratory studies of the role of bandwidth in surface transport and energy dissipation of deep-water breaking waves. *Journal of Fluid Mechanics*, 927:1–23.
- Stansell, P. and MacFarlane, C. (2002). Experimental Investigation of Wave Breaking Criteria Based on Wave Phase Speeds. *Journal of Physical Oceanography*, 32(5):1269–1283.
- Tan, P., Savelyev, I., Laxague, N. J., Haus, B. K., Curcic, M., Matt, S., Zappa, C. J., Mehta, S., and Wray, S. (2025). Wind-wave momentum flux in steep, strongly forced, surface gravity wave conditions. *Journal of Geophysical Research: Oceans*, 130:e2024JC021616.
- Tian, Z. and Choi, W. (2013). Evolution of deep-water waves under wind forcing and wave breaking effects: Numerical simulations and experimental assessment. *European Journal of Mechanics, B/Fluids*, 41:11–22.
- Tian, Z., Perlin, M., and Choi, W. (2008). Evaluation of a deep-water wave breaking criterion. *Physics of Fluids*, 20(6):066604.
- Tian, Z., Perlin, M., and Choi, W. (2010). Energy dissipation in two-dimensional unsteady plunging breakers and an eddy viscosity model. *Journal of Fluid Mechanics*, 655:217–257.
- Toffoli, A., Babanin, A., Onorato, M., and Waseda, T. (2010). Maximum steepness of oceanic waves: Field and laboratory. *Geophysical Research Letters*, 37(5):1–4.
- Touboul, J. and Banner, M. L. (2021). On the breaking inception of unsteady water wave packets evolving in the presence of constant vorticity. *Journal of Fluid Mechanics*, 915:A16.
- Touboul, J., Giovanangeli, J. P., Kharif, C., and Pelinovsky, E. (2006). Freak waves under the action of wind: experiments and simulations. *European Journal of Mechanics, B/Fluids*, 25(5):662–676.
- Wu, C. H. and Nepf, H. M. (2002). Breaking criteria and energy losses for three-dimensional wave breaking. *Journal of Geophysical Research*, 107(C10):3177.
- Xie, Z. (2017). Numerical modelling of wind effects on breaking waves in the surf zone. *Ocean Dynamics*, 67:1251–1261.
- Xu, Y., Liang, S., Sun, Z., and Xue, Q. (2022). A new spectral parameter to predict dominant wave breaking based on the jonswap spectrum. *Ocean Engineering*, 243:110332.
- Yousefi, K., Hora, G. S., Yang, H., Veron, F., and Giometto, M. G. (2024). A machine learning model for reconstructing skin-friction drag over ocean surface waves. *Journal of Fluid Mechanics*, 983:A9.
- Zhang, E., Wang, Z., and Liu, Q. (2024). A numerical investigation of momentum flux and kinetic energy transfers between turbulent wind and propagating waves. *Flow*, 4:E14.

Zou, Q. and Chen, H. (2017). Wind and current effects on extreme wave formation and breaking. *Journal of Physical Oceanography*, 47:1817–1841.